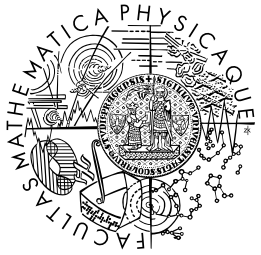

FACULTY
OF MATHEMATICS
AND PHYSICS
Charles University

MASTER THESIS

Bc. Jakub Bucko

Simulation and measurement of microchannel photomultiplier (MCP-PMT) treated by deposition of a protective atomic layer (ALD)

Institute of Particle and Nuclear Physics, Faculty of Mathematics and Physics,
Charles University

Supervisor of the master thesis: Mgr. Tomáš Sýkora, Ph.D.
Study programme: Particle and Nuclear Physics
Study branch: FCJFP

Prague 2023

I declare that I carried out this master thesis independently, and only with the cited sources, literature and other professional sources. It has not been used to obtain another or the same degree.

I understand that my work relates to the rights and obligations under the Act No. 121/2000 Sb., the Copyright Act, as amended, in particular the fact that the Charles University has the right to conclude a license agreement on the use of this work as a school work pursuant to Section 60 subsection 1 of the Copyright Act.

In ..... date ....

Author's signature

I would like to thank my supervisor Mgr. Tomáš Sýkora, Ph.D. for his help and patience. Also, I would like to thank my friends for their emotional support and additional help with the thesis.

Název práce: Simulace a měření mikrokanálkového fotonásobiče (MCP-PMT) ošetřeného depozicí ochranné atomové vrstvy (ALD)

Autor: Bc. Jakub Bucko

Ústav: Ústav částicové a jaderné fyziky, Matematicko-fyzikální fakulta, Univerzita Karlova

Vedoucí diplomové práce: Mgr. Tomáš Sýkora, Ph.D., Ústav částicové a jaderné fyziky, Matematicko-fyzikální fakulta, Univerzita Karlova

Abstrakt: Časové detektory budou tvořit zásadní roli v budoucím vývoji detekčních přístrojů, a to nejen ve fyzice vysokých energií. MicroChannel Plate PhotoMultiplier (MCP-PMT) je velmi rychlý (a velmi drahý) multifunkční fotonásobič a časový detektor. V současný době je tím nejlepším z hlediska časového rozlišení. Odezva MCP-PMT je nejen rychlá, ale je i odolná vůči vlivům magnetického pole. MCP-PMT se používá v mnoha současných i budoucích Time-of-Flight (ToF) detektorech. Vývoj MCP-PMT je časově a finančně náročný. Celý proces lze zjednodušit vytvořením počítačového modelu, který může být použit k simulaci chování MCP-PMT. Počítačový model může výrazně urychlit vývoj nových typů MCP-PMT vhodných pro signály s vysokou frekvencí opakování ($> 20\,\mathrm{MHz}$) a ušetřit mnoho laboratorního vybavení. Cílem mojí práce je vytvoření takového modelu.

Klíčová slova: MCP-PMT mikrokanálkový fotonásobič simulace

Title: Simulation and measurement
of microchannel photomultiplier (MCP-PMT) treated by deposition of a protective atomic layer (ALD)

Author: Bc. Jakub Bucko

Institute: Institute of Particle and Nuclear Physics, Faculty of Mathematics and Physics, Charles University

Supervisor: Mgr. Tomáš Sýkora, Ph.D., Institute of Particle and Nuclear Physics, Faculty of Mathematics and Physics, Charles University

Abstract: Time detectors will form a fundamental component in the further development of detection devices, not only in high-energy physics. The MicroChannel Plate PhotoMultiplier (MCP-PMT) is a very fast (and very expensive) multipurpose photomultiplier and time detector. It is currently the best available in terms of time resolution. In addition to the fact that its response is very fast, this response is also resistant to magnetic fields. The MCP-PMT is used in a number of current or upcoming Time-of-Flight (ToF) detectors. The development of MCP-PMTs is expensive and time-consuming. The process can be simplified by developing a computer model that can be used to simulate the behaviour of MCP-PMT. The model can greatly accelerate the development of a new type of MCP-PMT for high signal repetition rates ($> 20\,\mathrm{MHz}$) and save a number of laboratory experiments. An attempt to construct an MCP-PMT model is the goal of this work.

Keywords: MCP-PMT microchannel plate photomultiplier simulation

Contents

Introduction

High-energy physics experiments commonly require the detection of single photons. For example, the ATLAS Forward Proton (AFP) experiment uses Time-of-Flight (ToF) detector based on the Cherenkov light detection to improve signal-to-background ratio [1]. A single photon produces a weak signal, which requires specialized equipment such as a PhotoMultiplier Tube (PMT) to detect the light. Usually, a PMT consists of an evacuated glass tube with a photocathode at one end and a collector anode at the other end. Between the electrodes, a system of different electrodes called dynodes is placed. A high voltage is applied across all electrodes. When a photon arrives at the PMT and hits the photocathode, an electron (a so-called photoelectron) is released and is accelerated by the high voltage. When the electron hits a dynode, a secondary emission occurs, and more electrons are released. In this way, the weak signal is amplified and finally collected by the cathode. Such PMTs have serious disadvantages. Their performance is significantly affected by magnetic fields [2], and the time characteristics of the PMTs limit their use in ToF detectors. According to [3], the transit time spread (the time width of the output signal) of the conventional PMTs is $\sim 1\,\text{ns}$. The AFP experiment requires a detector with a time resolution of 10 ps or better, which means that the conventional PMTs cannot be used. In the 1960s, MicroChannel Plate (MCP) was introduced [4]. These devices can replace the dynode structure and significantly improve the performance of photomultipliers. For example, they are significantly more resistant to magnetic fields, and their time characteristics are better than conventional PMTs [3]. The development of MicroChannel Plate PhotoMultiplier Tube (MCP-PMT) technology continues; MCPs have problems, such as gain saturation, that need to be solved. However, the development requires a lot of resources and manpower, and the behaviour of MCPs is hard to measure. These problems were even more pronounced in the past, and so early after the development of the first MCPs, a novel approach was used to study them. In the 1970s, the first computer simulations of MCP-PMT behaviour were done [5]. The simulations allow for studying the inner microscopic behaviour and could, in theory, predict the outcome of signal detection. Using simulations, new MCP-PMTs can be designed and tested before they are manufactured. This can significantly reduce the cost of development and speed up the whole process.

This work explores different possibilities and techniques for creating such simulations. An attempt to develop an entirely new simulation of MCP-PMTs was made, which includes the creation of a technique to optimize and speed up the simulations in a special case. Also, a simple simulation using existing commercial simulation software was created. The results of the simulations were compared with each other and with the results of previously done simulations.

The first chapter of this thesis describes the microchannel plate and provides some insight into the history of its development. It describes the advantages and the disadvantages of MCPs and mentions different ways that the problems can be mitigated. The second chapter is devoted to the simulations. It provides a description of two new models and their results. Finally, the use of commercial software is explored and compared with the developed simulation code.

Used notation

The following mathematical notation is used in this thesis:

- Unit vectors are denoted by a hat: $\hat{y}$.
- All other vectors are denoted with an arrow: $\vec{x}$.
- All points are represented by bold letters: $\mathbf{S}$.
- Matrices are represented by a horizontal line: $\overline{M}$.

1. Theory

1.1 Microchannel plate

A microchannel plate (MCP) is a lead glass plate with an array of microscopic channels called microchannels. Figure 1.1 shows a drawing of a MCP. Depending on its size, a MCP can contain from 10^4 to 10^7 microchannels parallel to each other [4]. The main characteristics of the microchannels are their diameter and length-to-diameter ratio; typical microchannel diameter is 10 µm to 100 µm and the typical length-to-diameter ratio is ~ 40. Microchannels of the first MCPs were perpendicular to the MCP face, but nowadays, they are at a small angle (see Section 1.6 for more information).

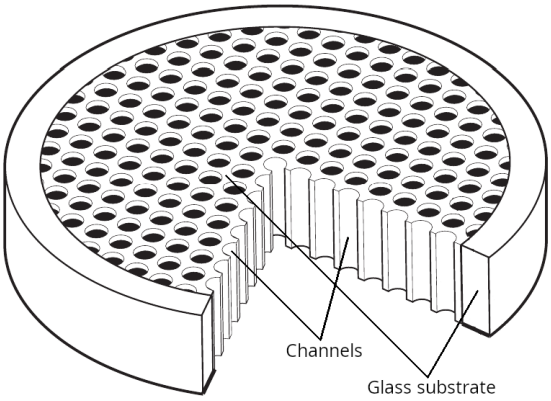

Figure 1.1: Drawing of a microchannel plate. The plate is usually made out of lead glass. The faces of the plate are covered with conducting material to form electrodes. Edited the original figure from [3].

Microchannel plates were developed from macroscopic channel multipliers. These were small tubes with a diameter of a few millimetres used as electron multipliers. It was found [6] that the multiplication properties of the channel multipliers do not depend on the whole geometry but only on the length-to-diameter ratio, which led to the development of smaller channel multipliers. Soon there were attempts [7] to stack the multipliers into arrays and use them as image intensifiers.

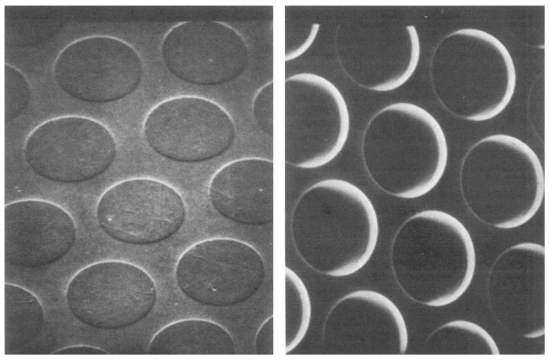

Figure 1.2: Scanning electron microscope image of an unprocessed wafer (left) and final MCP (right) [4].

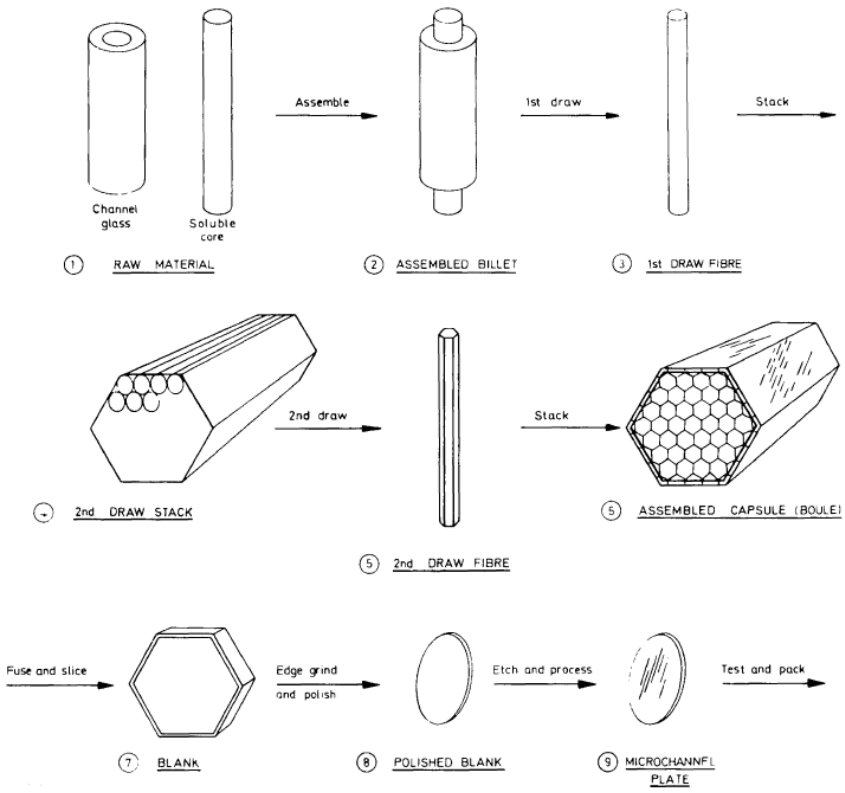

Figure 1.3: Original MCP manufacturing process diagram [8]

As the channel multipliers were becoming smaller, a new manufacturing process was developed, and the first MCPs were made. According to [4] MCPs were manufactured by the etchable core technique, the diagram of which is in Figure 1.3. The channels of an MCP are made from glass fibres. The structure of the fibres consists of an etchable core and an outer layer made out of lead glass. The material of the core has to be such that it can be etched by a chemical that does not dissolve the lead glass. The fibres are put together to form a hexagonal array. Multiple such arrays are stacked again, and a multi-fibre structure is created. Finally, these structures are put together and fused into a boule, which is then sliced into thin wafers; the slicing is usually done at an angle to create MCPs with channels that are not perpendicular to the MCP faces. The wafers then need to be polished, edged and bevelled. After that, the inner core of the fibres is etched out, and the wafers are chemically treated to improve their secondary emission characteristics. The wafers are then put into a hydrogen furnace, where they are heated and reduced. The lead oxide in the glass is converted to semiconducting lead. The temperature must be carefully controlled, because if the temperature is too high, an agglomeration process takes over the formation of the semiconducting lead. Finally, conducting material is deposited onto the faces of the wafer. This creates a parallel connection between the channels, and the layers are used as electrodes for applying a bias voltage. The basic steps needed for the manufacturing of an MCP were presented above. The unprocessed wafer and the final MCP structure can be seen in Figure 1.2. The typical resistance between electrodes is on the order of $10^9\,\Omega$. However, the resistance is substantially affected by temperature. The temperature coefficient of the glass is negative [9].

This means that the resistivity of the glass decreases with temperature. This can lead to a feedback reaction: as the MCP is heated, the resistivity drops and more current can flow through it. This leads to subsequent heating, a higher resistivity drop, and so on. Eventually, this leads to the destruction of the microchannel plate.

The manufacturing process described above was used to create MCPs before the year 2010, when the properties of the MCPs made by this process were no longer sufficient, and new processes and technologies had to be developed. More about these new MCPs can be found in Section 1.7.

Photomultiplier tubes made using microchannel plates are quite different in structure and operation and can offer features and performance superior to dynode PMTs, like:

- fast time response and high time resolution: Typical transit time is $\sim 100\,\text{ps}$, and the transition time spread can be $\sim 45\,\text{ps}$. Newer MCP-PMTs can have even better time characteristics with time resolution $\sim 10\,\text{ps}$ [3].

- high spatial resolution in two spatial dimensions. The resolution depends on the construction of the collector anode, but in theory, each microchannel could act as a single pixel.

- robustness to a magnetic field. Some MCP-PMTs can withstand a magnetic field up to 5 T before their gain drops significantly. This is discussed in greater detail in Section 1.5.

- MCPs are able to detect charged particles, electromagnetic radiation ranging from ultraviolet to gamma radiation, and neutrons [3]. However, the final sensitivity of an MCP-PMT depends on the transmittance of the used window.

There are two main modes of MCP operation. The first one is the DC mode when there is a light shining continuously on the MCP-PMT. This mode is typical for image intensifiers like the ones used in night vision gear. The second mode is the pulsed mode when the light hits the MCP-PMT in a pulse. The pulse can be a single photon released from some process in a experiment or it can be a laser pulse.

1.2 Structure of MCP-PMT and power supply

Figure 1.4 is a drawing of a cross-section of a typical MCP-PMT. The drawing shows that the PMT consists of a window followed by a photocathode used to convert detected photons to electrons, a pair of MCPs, and a collector anode. The typical distance between the first MCP and the photocathode is $\sim 2\,\text{mm}$ [3]. There can also be a thin ion barrier between the first MCP and the photocathode to reduce the number of positive ions. However, this barrier reduces the quantum efficiency. The PMT in the drawing also uses MCP with slanted microchannels oriented such that they create a V shape. The collector anode can be either a single piece, or it can be segmented to achieve 2D detection. An MCP-PMT has to be properly powered. Each component needs to be supplied with the correct

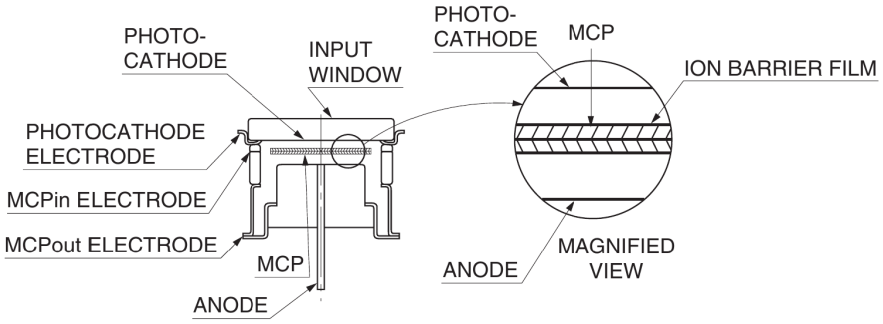

Figure 1.4: Drawing of a MCP-PMT cross-section [3].

voltage such that the optimal voltage difference between the MCPs, the photocathode and the anode is achieved. The voltage difference between the MCPs called bias voltage needs to be high enough to generate strong electric field. The field is uniform inside the microchannels, but the geometry of the microchannels and different potentials between the MCP layers cause a deformations at the ends of the channels. These deformed fields are called fringe fields. They significantly alter the motion of the electrons and can have an effect on performance [10].

A proper power supply and voltage divider has to be used to power an MCP-PMT. Figure 1.5 shows an circuit diagram of such a voltage divider. The

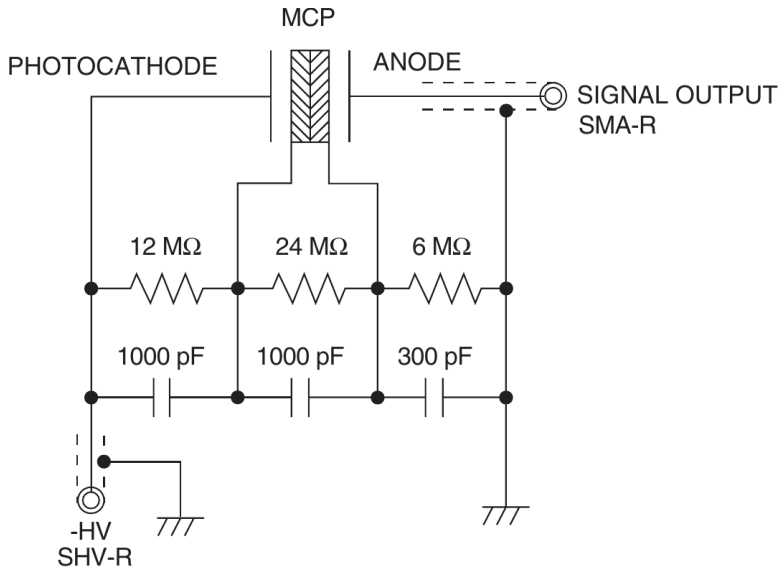

Figure 1.5: Circuit diagram of voltage divider used to power MCP-PMT [3].

power supply and the voltage divider have to supply high voltages. The voltage on the MCPs is in the order of 1 kV, and the voltage between MCP and photocathode can be as high as 300 V [11].

1.3 Saturation

For MCP-PMT to be a useful tool, one expects that its output is proportional to the input signal. For example, when an MCP-PMT is used in pulsed mode, the output signal should rise with a higher pulse rate. However, the output signal saturates and stops changing if the pulse rate is high enough. Three types of

saturation effects are described in the literature: space charge saturation, wall charge saturation, and current saturation [12].

The space charge saturation occurs because of the distribution of particles inside the channel. As the signal propagates through, new electrons are created, and the density of the electron cloud increases. A radial electric field is created, which acts on the newly created particles. Because of the field, the particles cannot travel far from the wall, and they cannot gain enough energy to create new secondary electrons. After the collision, the electrons are either absorbed or reflected. This leads to an equilibrium state in which the number of new electrons is equal to the number of absorbed electrons. The coefficient of secondary emission is effectively equal to unity [13].

The wall charge saturation occurs because of positive charge buildup at the end of the channel. The secondary emission of electrons, which is responsible for signal amplification, removes electrons from the wall. Due to the high resistance of the wall, the strip current that replenishes the wall with new electrons is small. The small current means that it takes some time to restore the electron content of the wall. When the pulse rate is higher than this dead time or recovery time, the positive charge appears [3]. The charge then distorts the electric field in the channel. This distortion leads to decreased secondary emission yield and affects the output signal. There is a simple relation for the dead time:

$$\tau_{\mathrm{d}} = \frac{Q_{\mathrm{out}}}{I_{\mathrm{s}}}, \tag{1.1}$$

where Q_{out} is the charge of the output and I_{s} is the strip current [3].

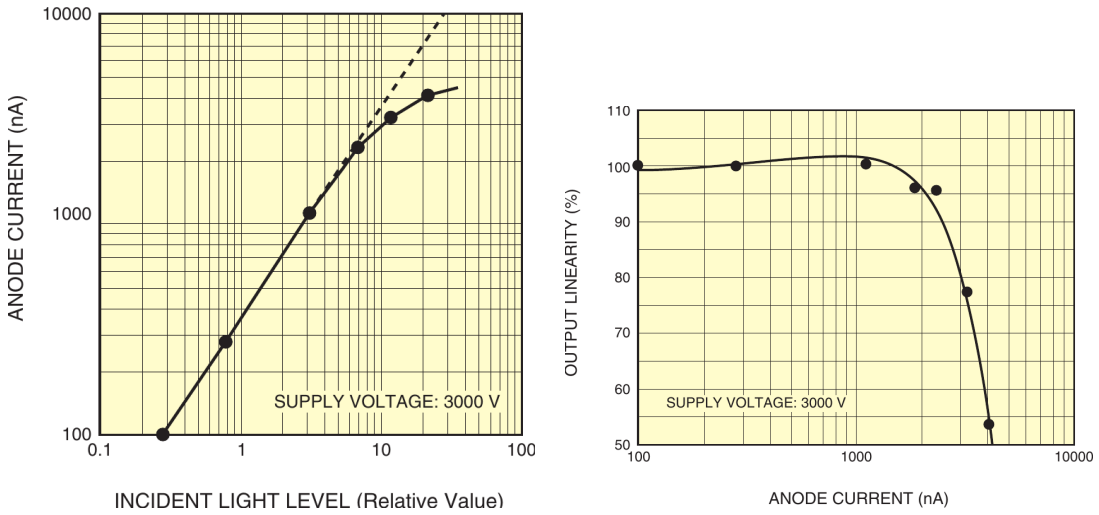

Figure 1.6: The saturation characteristic of MCP-PMT caused by DC light [3].

The current saturation effect is similar to the wall charge saturation. It occurs in a continuous DC mode. The effect is also caused by the high resistance of the wall material, which limits the maximum output current available. Figure 1.6 demonstrates this effect. As the input current raises, the output current is increasing, but at some point the output current starts to get saturated. In the region where the output current is saturated, the electric field at the end of the channel has decreased. This is caused by variations in potential at the channel end, which results from releasing a large amount of electrons from the wall. The

saturation starts to occur when the output current is around 7 % of the strip current [3].

The effect of the gain saturation can be seen in Figure 1.7 with the gain vs applied bias voltage characteristic of an MCP-PMT. One can see how the MCPs get saturated with higher bias voltage as this creates a stronger electric field, which leads to higher electron energies and higher secondary electron yield. Also, the photomultiplier with a single MCP saturates quicker. This is due to the ion feedback effect, which is reduced in a chevron configuration. The second configuration also has the advantage of a higher overall gain.

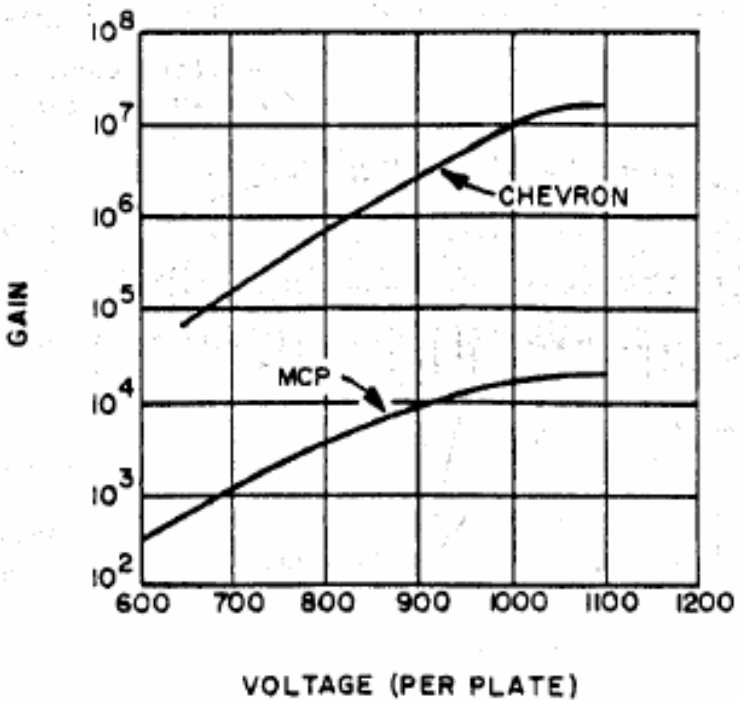

Figure 1.7: Gain vs bias voltage characteristic of PMT with single MCP and with two MCPs in a chevron configuration [4].

These saturation effects significantly impact the performance and usability of MCP-PMTs, which is a strong motivation to mitigate these effects. One way that one can deal with saturation is to operate the MCP-PMT in a non-saturated region. However, such an approach is unreachable, because the background in a lot of experiments is high enough to create lot of pulses that saturates the photomultipier. Another way to suppress the saturation is to put multiple layers of MCPs inside one photomultiplier. A typical MCP-PMT has at least two microchannel plates, but photomultipliers with three plates have also been developed [14]. Another way is to coat the walls with some other material.

1.4 Pulse creation and secondary emission

The basic working principle of MCP-PMTs is that a photon kicks out an electron from the photocathode which is then accelerated and multiplied by MCP. This would mean that a single pulse could be expected. In reality, there are four types of pulses that can be generated [11]. All the types are illustrated in Figure 1.8.

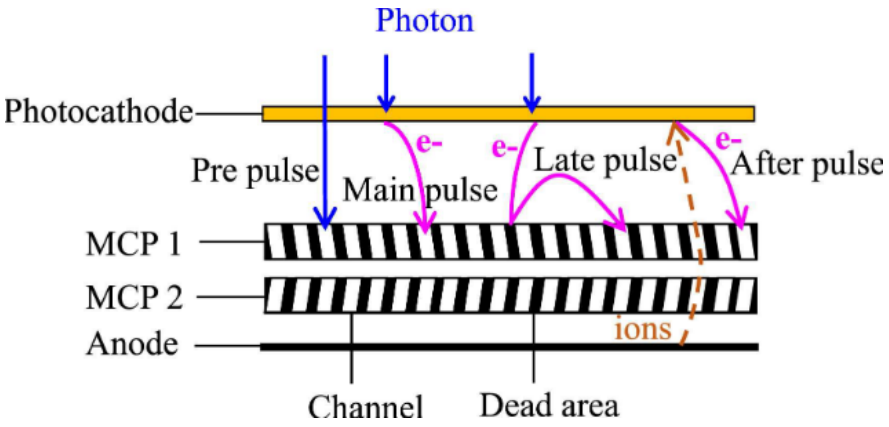

Figure 1.8: Illustration of creation of MCP-PMT signal [11].

The first pulse type is the so-called pre-pulse which occurs when a photon passes through the photocathode and hits the first MCP. Electrons are then emitted from the MCP instead of the photocathode. One of the main characteristics of a photocathode is quantum efficiency. It is defined as the number of emmited photoelectrons divided by the number of incident photons. The quantum efficiency of photocathodes is less than 100 %, nowadays the maximum is $\sim 40\,\%$ [3]. The low quantum efficiency is the reason why the photons can pass through the photocathode.

Then, there is the main pulse created by the mechanism described at the beginning of this section. Usually, 40 % to 60 % of the electrons emitted from the photocathode contribute to this pulse [11]. This pulse creates the strongest signal.

The rest of the photoelectrons can scatter off the face of the first MCP and create secondary electrons. They can either scatter more or enter a microchannel and contribute to the late pulse, which is the third pulse type. This pulse can create problems when the MCP-PMT is used for counting electrons because it worsens the time resolution. This pulse can be suppressed by a strong electric field near the MCP face [11].

As was mentioned before, the multiplication of the electrons is realised through secondary emission from the wall material. The main characteristic of the secondary emission is the Secondary electron Emission Yield (SEY) defined as

$$\delta = \frac{I_s}{I_p}, \tag{1.2}$$

where I_p is the current of electrons colliding with the material, and I_s is the current of all electrons that are either scattered or leave the material. The dependence of δ on the energy of the primary electrons is depicted in Figure 1.9a. The value of SEY rises with higher primary energy until it reaches maximum δ_m at energy E_m, then the SEY starts to decrease. The dependence can look counter-intuitive as one would expect the yield to be higher with higher primary energy. However, the energy of secondary electrons is low, the maximum is $\sim 50\,\mathrm{eV}$ [15]. This means that the electrons cannot travel long distances. When the energy of the primary electrons is low, the penetration depth is also low, and the secondary electrons can escape from the material. But as the primary energy increases, the primary electrons can penetrate the material deeper and the electrons at that

depth can have a problem travelling on the surface of the material [15]. The plot in Figure 1.9a also shows that there are two values of the primary energy E_I, and E_{II} at which the SEY is equal to one. These energies are called the first and the second crossover energies.

The source of the current I_s can be split into three components: true secondary electrons, elastically scattered electrons, and rediffused electrons. The distinction between the components is based on the energies of the electrons; Figure 1.9b shows the energy spectrum of SEY with the three components labelled. In this

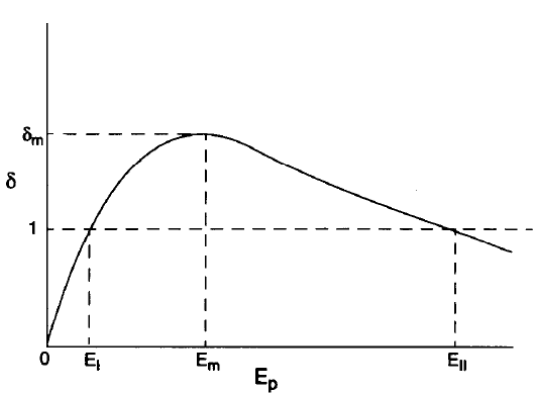

(a) The dependence of the total secondary electron emission yield on primary electron energy [15].

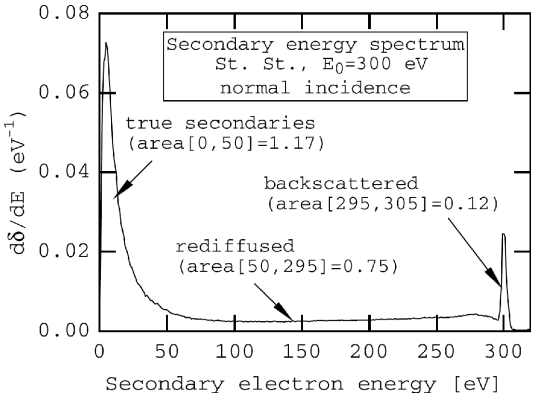

(b) Energy spectrum of secondary electron emission yield [16]. The plot also shows the three components of the total SEY. The yield of each component is the area under the curve in the energy region denoted by the values in the brackets.

Figure 1.9: The properties of secondary electron emission.

work, a probabilistic model developed by Furman and Pivi [16] is used to simulate the secondary emission. In the paper [16], the energy distribution function and Probability Density Function (PDF) is derived for each component. The PDF of a component corresponds to the component's probability of emitting an electron of the component. Both functions depend on the primary energy and the collision angle. The model requires a significant number of parameters, the values of which have to be obtained by fitting the functions to experimental data. The parameters for copper from Table 1.1 were used in this work for testing of the model and the simulations. Also, the parameters for the LHC beam screen obtained from [17] were tested, but they provided almost identical results.

1.5 Magnetic field tolerance

Microchannel plates can withstand strong magnetic fields without a significant decrease in gain. However, the tolerance strongly depends on the MCP geometry and the magnetic field's orientation. It was shown that the influence of a transverse magnetic field is much stronger than the influence of an axial magnetic field. Some MCP can operate in axial magnetic field up to 5 T but can tolerate transverse field only up to ~ 2 T [18]. An axial magnetic field can even improve the gain of MCP to a certain degree because the gain dependence on the axial

Parameter	Value	Description
α	1	
$P_{1,e}(\infty)$	0.02	Prob. of emission of backscattered e^- at $E_0 \to \infty$
$\hat{P}_{1,e}$	0.496	Prob. of emission of backscattered e^- at $E_0 = \hat{E}_e$
$\hat{E}_e$	0	Incident energy for which $\delta_e(E_0, 0)$ is at maximum
W	60.86 eV	
p	1	
σ_e	2 eV	Deviation of the energy probability function $f_{1,e}$
e_1	0.26	
e_2	2	
$P_{1,r}(\infty)$	0.2	Prob. of emission of redifused e^- at $E_0 \to \infty$
E_r	0.041 eV	Incident energy for which $\delta_r(E_0, 0)$ is at maximum
r	0.104	
q	0.5	
r_1	0.26	
r_2	2	
$\hat{\delta}_{ts}$	1.8848	Peak value of SEY function $\delta_{ts}(E_0, \theta_0)$
$\hat{E}_{ts}$	276.8 eV	Incident energy for which $\delta_{ts}(E_0, \theta_0) = \hat{\delta}_{ts}$
s	1.54	
t_1	0.66	
t_2	0.8	
t_3	0.7	
t_4	1	
$\hat{E}_t$	271 eV	Incident energy for which $\delta(E_0, \theta_0) = \hat{\delta}_t$
$\hat{\delta}_t$	2.1	Peak value of the total SEY δ

Table 1.1: Parameters of the Furman-Pivi model used for testing. Obtained from TABLE I. from [16].

magnetic field shows a rising tendency. However, the dependence has a maximum after which the gain is rapidly decreased [19, 20]. An axial magnetic field can also improve spatial resolution and reduce charge-sharing effects [21]. The tolerance can be improved by changing the geometry of MCP and whole MCP-PMT by decreasing the diameter of the microchannels and by changing the gaps between MCPs and anodes [18, 19].

1.6 Ion feedback and damage

The electrons accelerated by the electric field are responsible not only for the creation of secondary electrons but also for the creation of positive ions. This is an undesirable effect for operation of an MCP. The ions travel in the opposite direction to the electrons. They are also accelerated by the field. They can hit the wall of a channel and create new secondary electrons, or they can propagate back to the photocathode, where they produce new electrons after collision. At first sight, this can be seen as a good thing. There is more electrons, which means higher gain. However, the ions actually bring additional noise to the output signal. The presence of additional electrons also means that the MCP operates

in the saturated mode sooner. The electrons created in the collisions of the ions with the photocathode are usually not part of the main output signal, but they are responsible for after pulses. These are the source of the additional noise. Also, the bombardment of the photocathode by the ions significantly reduces its quantum efficiency and its lifetime. This, in turn, reduces the lifetime of the whole MCP-PMT as the photocathode cannot be replaced. The lifetime is the time it takes for the quantum efficiency of MCP-PMT to drop to 50 %. Usually, it is expressed as collected anode charge per unit area integrated over time and given in units of $\mathrm{C\,cm^{-2}}$. The reduced lifetime can be a problem for experiments with high pulse rates.

The positive ions are either released from the walls after an electron collision, or they are created by ionization of a residual gas [22]. The residual gas is mostly composed of carbon dioxide and monoxide, and water, according to [23]. According to the paper, these gases can be left inside a PMT from the manufacturing of the photocathode. However, the main result of the paper is that the gases do not have to be ionized to damage the photocathode. The interaction of the neutral CO_2 and H_2O particles with GaAs photocathode can significantly lower its quantum efficiency even at low gas pressure.

The ion effects can be mitigated by making the microchannels tilted, usually by $\sim 15°$ In such a configuration, ions are pushed towards the walls, which lowers the probability of ions hitting the photocathode. However, this is usually not sufficient and other techniques have to be implemented. The addition of an aluminium ion barrier between the photocathode and the first MCP helps to reduce the ion damage, but it lowers the quantum efficiency of the MCP-PMT.

1.7 MCPs with atomic layer deposition

The ion damage effect and the overall short lifetime makes the classical MCPs almost unusable for high-energy physics experiments, as the photomultipliers would have to be frequently replaced, which is impractical and not financially viable. According to [24], the typical lifetime of a classical MCP-PMT is $0.1\,\mathrm{C\,cm^{-2}}$. This value is quickly exceeded in the high background environment of high-energy physics experiments.

To improve the lifetime, a new type of MCPs was developed. The MCPs of this new type are treated by the Atomic Layer Deposition (ALD) process to deposit layers of different materials onto the walls of microchannels. The process usually involves the deposition of three layers: the resistive layer, the secondary emission layer and an electrode layer. Figure 1.10 shows the structure of ALD-treated MCP. The functions of the different layers can be guessed from their names. The emission layer is responsible for the multiplication of electrons via secondary emission. The resistive layer is designed to conduct the strip current that replenishes the lost electrons. The electrode layer is deposited only to the faces of MCP, and it is used as electrodes for the bias voltage. The emissive layer is usually made from a material with a high secondary emission coefficient. This means that the bias voltage can be lower while the gain would be the same. With lower bias voltage also, the energies of the electrons are lower, which means that their ability to ionize the residual gas is lower. This results in the reduction of the positive ions and extended MCP-PMT lifetime [24]. Apart from the im-

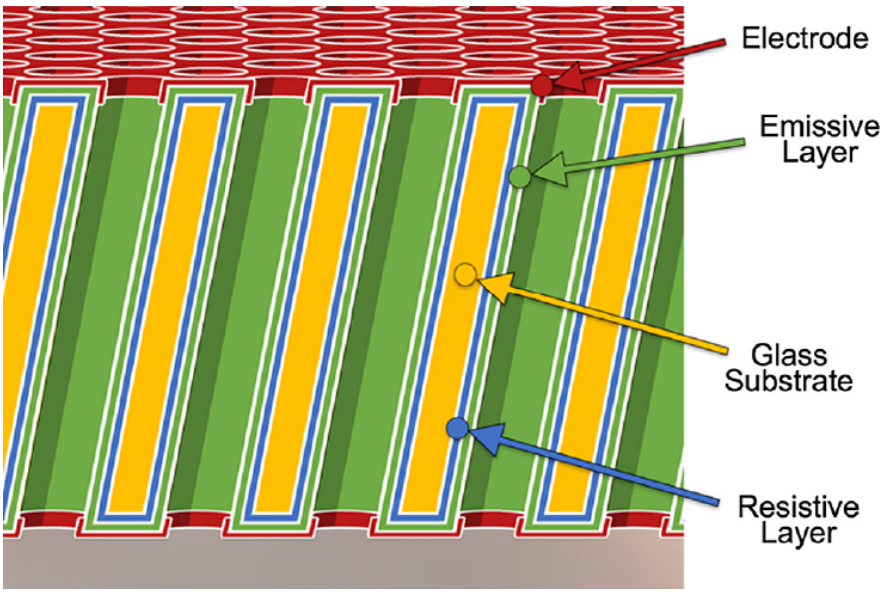

Figure 1.10: The different layers of ALD treated MCP [25]. The conventional MCP would contain only the glass substrate and the electrodes. The inclusion of additional layers allows for different substrate materials.

proved lifetime, the ALD process also improves the gain and quantum efficiency of MCPs [22, 25]. The use of three distinct layers with their own functions means that each layer can be changed and engineered separately to tweak the performance of an MCP. Because the secondary electron emission is not performed on the emissive layer of an ALD MCP, the lead glass substrate can be replaced with different glass materials, for example, borosilicate glass can be used. The ALD process also allowed requires an improved manufacturing process [26].

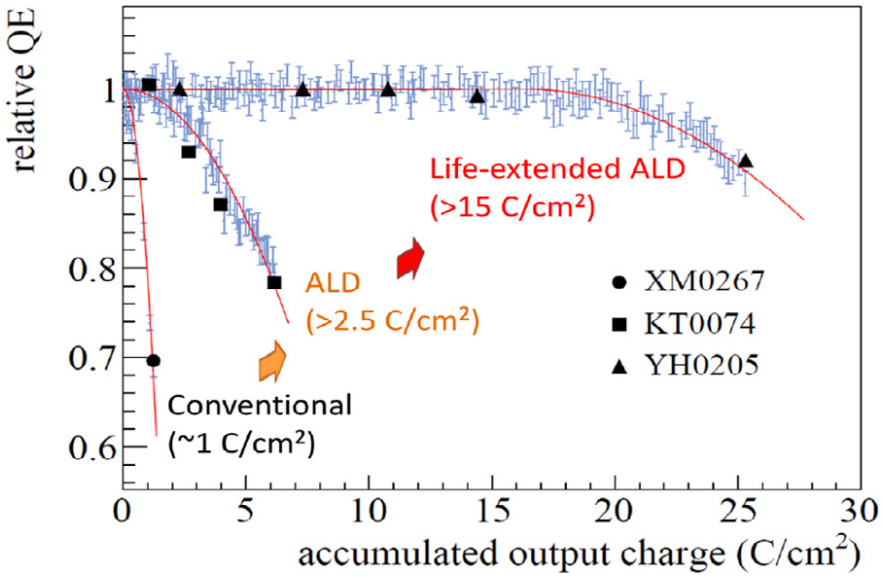

Figure 1.11: Plot showing the lifetime improvement of MCP-PMT used in the Belle II iTOP detector [27].

The new MCP-PMTs improved by ALD are used in various experiments. For example, an array of MCP-PMTs is used as part of the Belle II iTOP Time-Of-

Propagation detector [28]. The assembly consists of a quartz radiator connected to the PMT array at one end. The quartz radiator is consists of two quartz bars responsible for generating Cherenkov light. The PMTs are used to detect the Cherenkov ligh. Initially, the PMTs used an Al layer to reduce the number of ions reaching the photocathode [29], but later an ALD MCPs were used. The improvement in the lifetime can be seen from Figure 1.11. Another experiment

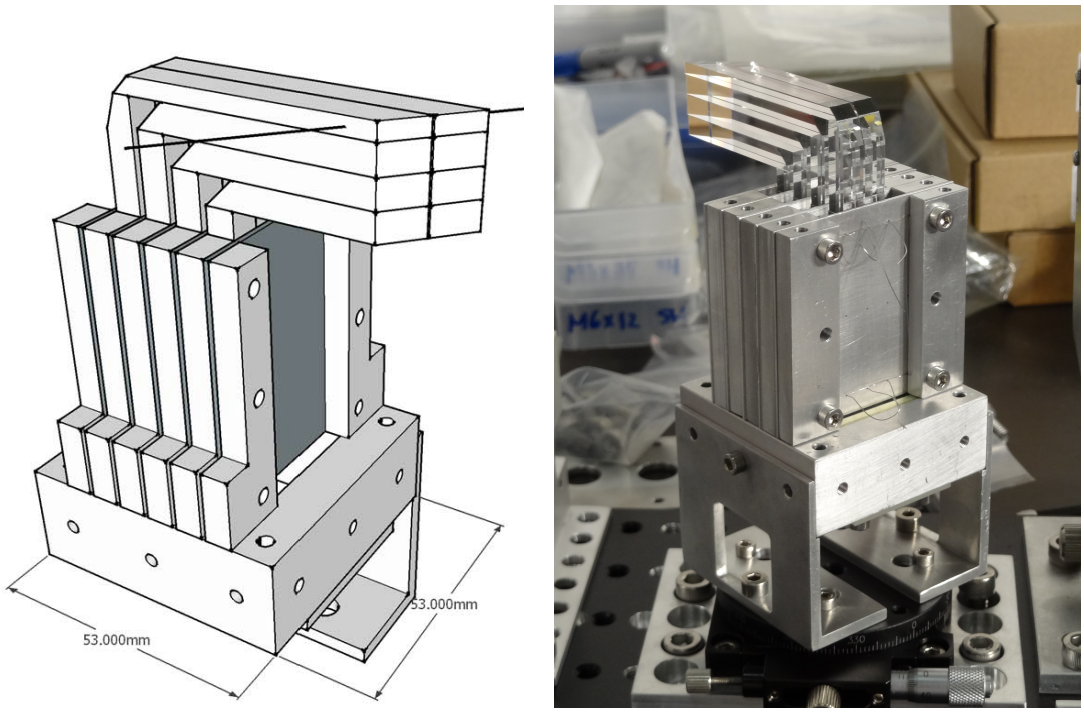

(a) Drawing of a prototype of the LQBars assembly. The black line that intersects the LQBars represents a proton trajectory.

(b) Photo of the assembly before test beam installation in November 2014.

Figure 1.12: The LQBar assembly for the first generation of AFP ToF detector [1]. Cherenkov radiation is generated in the bars and guided into the MCP-PMT that would be mounted under the bars during normal operation.

that uses MCP-PMTs treated with ALD is the PANDA (AntiProton Annihilation at Darmstadt) experiment [30]. The MCP-PMTs are used in their DIRC detector. ALD-treated MCP-PMTs are also used in AFP experiment [1] as part of their ToF detector. The ToF detector is a Cherenkov light detector consisting of a matrix of LQBars connected to an MCP-PMT at one end. The whole detector is then put into a Roman pot, which is a cylindrical enclosure that can be inserted into the LHC beampipe. Figure 1.12 shows the LQBars assembly. The LQBars are used to create the Cherenkov light and to guide it into the MCP-PMT. The anode of the MCP-PMT is segmented to create 4x4 pixels, and the LQBars are aligned such that two bars belong to one pixel. The detector is used to reduce pile-up background, which requires a high time resolution of at least 10 ps. Moreover, the system has to be reliable and robust. MCP-PMTs are capable of satisfying the high time resolution requirement. However, the classical MCPs would not be robust enough, so ALD-coated MCPs must be used. The detector

uses MCP-PMTs known as mini-Planacon, developed by Photonic Corporation. The improved performance of the MCP-PMT can be seen in Figure 1.13.

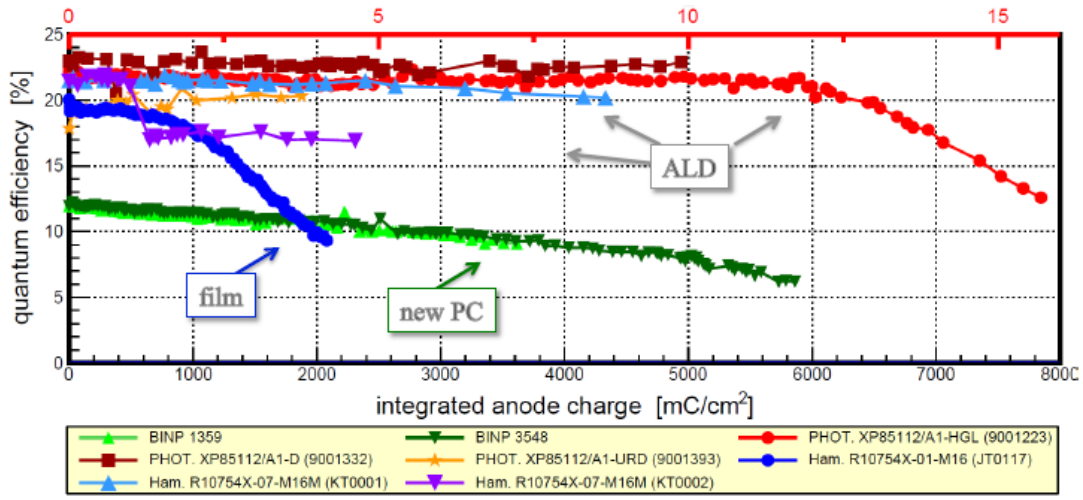

Figure 1.13: Comparison of lifetime of various MCP-PMTs [1].

2. Simulations

2.1 Introduction

The most important tools of physics are experiments and their measurements. They are used to discover new phenomena, verify or disprove predictions, test and calibrate equipment. However, sometimes it can be difficult and expensive to do an experiment, for example, if one wants to study some chaotic system or when one is developing new technology and needs to test many prototypes. In such cases, one can resort to simulations, model the problem using the knowledge of physical laws, and do the "experiment" on a computer. A computer model that reflects reality sufficiently can save time, human resources and money. It is simpler and cheaper to repeat a simulation than a physical experiment. When developing an apparatus, for example an MCP-PMT, all that needs to be done to see the response of the PMT to a particular signal is to tweak the parameters of the simulation and run it. Using computer models, one can build the actual MCP-PMT later when the simulations show the desired behaviour of the MCP-PMT.

2.2 Transmission line modeling

Transmission Line Modeling (TLM) is used to study the macroscopic aspects of a system. As the name suggests, the method is based on a modeling method developed for modeling and solving transmission lines problems. In the simplest form a problem is modeled by replacing the complex system by a relatively simple network of lumped components like resistors, capacitors, and inductors. Then the Kirchhoff's current and voltage laws are used to derive equations that solve the system [31]. A simulation then typically consists of numerically solving the derived equations. This method was already used for modeling MCP behaviour, the first models were developed by Giudicotti [32–34], later some models were developed by Shikaliev [12], and Berkin and Vasil'ev [35, 36].

2.2.1 Giudicotti's model

The model developed by Guidicotti [34] was tested to see its usability. The goal of the model is to provide a time dependent model of saturated multiplier gain. It tries to consider the charge effects that occur in the MCP by modelling the multiplier as a network of capacitors and resistors. This leads to an iterative method of calculating the gain as function of time and position along the channel:

$$g_0(x,t) = e^{Gx} \tag{2.1}$$

$$\left(\frac{Q(x,t)}{Q_S}\right)_n = \frac{1}{Q_S}\int_0^t i_0(t')g_n(x,t')dt' \tag{2.2}$$

$$\left(\frac{Q_{W0}(t)}{Q_S}\right)_n = -\frac{Q_0(t)}{Q_S} + \frac{1}{L}\int_0^L \left(\frac{Q(x',t)}{Q_S}\right)_n dx' \tag{2.3}$$

$$\psi_n(x,t) = \psi(x,0) + \frac{Q_0(t)}{Q_S} + \left(\frac{Q_{W0}(t)}{Q_S}\right)_n - \left(\frac{Q(x,t)}{Q_S}\right)_n \tag{2.4}$$

$$g_{n+1}(x,t) = \exp\left\{Gx + \int_0^x \ln[1+\psi_n(x',t)]dx'\right\} \tag{2.5}$$

where L is the length of a microchannel, and G is logarithmic gain, a parameter that needs to be measured. When an unsaturated MCP-PMT is simulated, the $\psi(x,0)$ value is set to zero for every x. The process works by taking the initial value (2.1) and calculating the equations (2.2) - (2.5). Then, the process is repeated using the new values of $g(x,t)$ until a desired precision is reached.

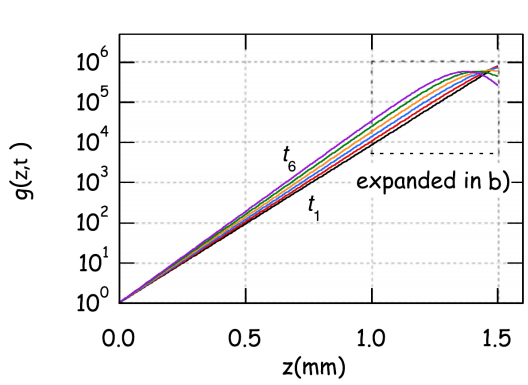

(a) The relation between the MCP-PMT gain and position along the channel. Edited.

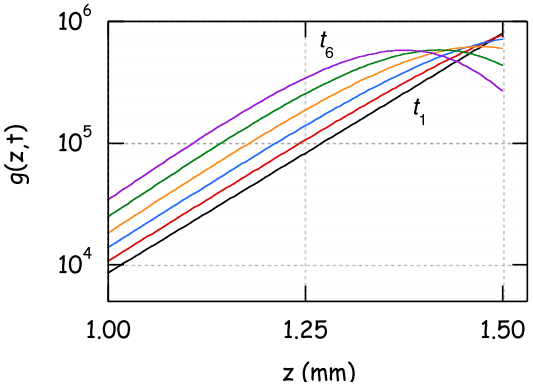

(b) Cutout from the left figure.

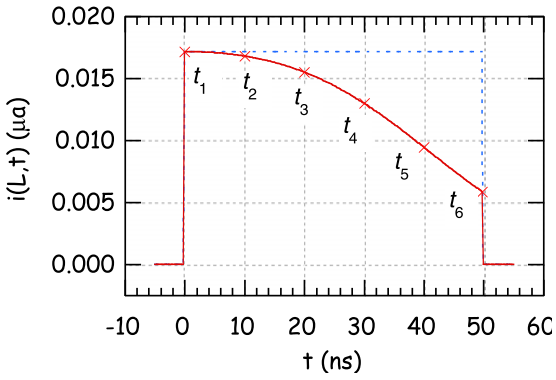

(c) The shape of the output signal.

Figure 2.1: Original results from [34]. The curves in (a) and (b) were calculated every 10 ns at times marked in (c). Text in (a) edited for consistency.

This work tried to reproduce the result of the paper [34] by implementing the equations (2.1) - (2.5) and calculating the gain. The original results are

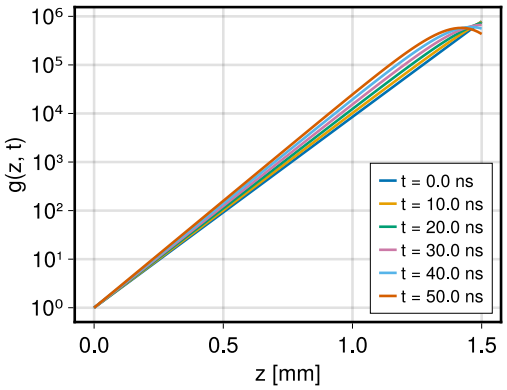

(a) The relation between the MCP-PMT gain and position along the channel

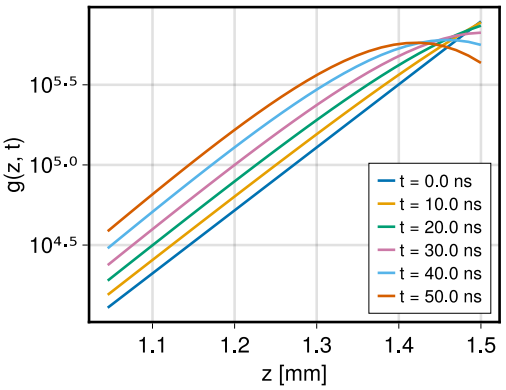

(b) Cutout from the left figure.

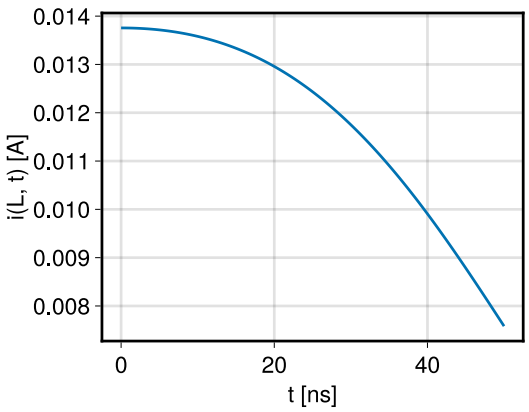

(c) The shape of the output signal.

Figure 2.2: Results from the implementation of the TLM model used for this thesis.

in Figure 2.1 and the recreated results are in Figure 2.2. By comparing the plots, it can be seen that the results match very well. This means that the new implementation of the TLM model can be used for simulating various multipliers. However, the whole model has a flaw which renders it unusable. In order to derive equations (2.2) - (2.5), the author assumed that the signal length, i.e. the time width of $i_0(t)$ is much longer than the transition time. The typical number of photoelectrons entering an MCP is around 15 - 45 photoelectrons. As was mentioned before, the typical MCP has around 10^6 microchannels, which means that one can expect no more than a single photoelectron to enter a microchannel. This is equivalent to the delta function as an input signal: $i_0(t) = \delta(t)$. This means that the signal length is zero, and the assumption is broken.

Nevertheless, it was investigated if the model could be used to calculate the wall charge as a function of time and space, and use the values in another simulation. The equation (21) in the paper [34] gives this relation between the current flowing in the wall, the input signal current and the signal current:

$$i_w(x,t) = i_{w0}(t) + i_0(t) - i(x,t), \tag{2.6}$$

where $i_w(x,t)$ is the wall current, $i_{w0}(t)$ is the wall current at the beginning of the

channel. $i_0(t)$ is the input current and $i(x,t)$ is the signal. Integrating equation (2.6) over time gives the relation for the wall charge $Q_w(x,t)$:

$$Q_w(x,t) = Q_{w0}(t) + Q_0(t) - Q(x,t). \tag{2.7}$$

The quantities $Q(x,t)$ and $Q_{w0}(t)$ are part of the iterative process and can be calculated using the equations (2.2) and (2.3) respectively. The value of $Q_0(t)$ is obtained by numerical integration of the input signal. Using equation (2.7) and the data obtained from calculating the gain, a numerical result for $Q_w(x,t)$ was calculated. The result is plotted in Figure 2.3c. However, having it as a mathematical expression is more practical, so a surface was fitted onto the data. In Figure 2.3a, one can see how the value of $Q_w(x,t)$ changes with time at

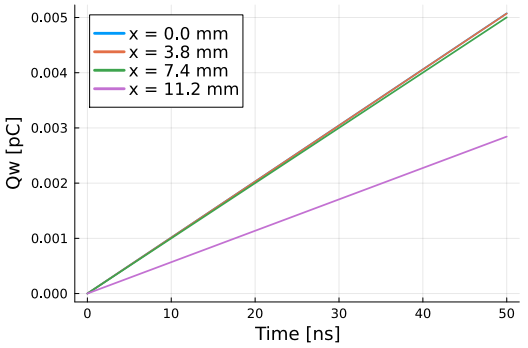

(a) Behaviour of Q_w with respect to time.

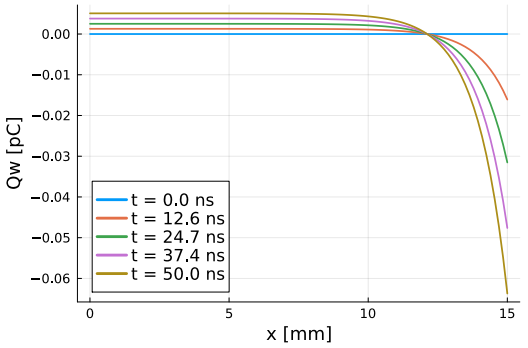

(b) Behaviour of Q_w with respect to x.

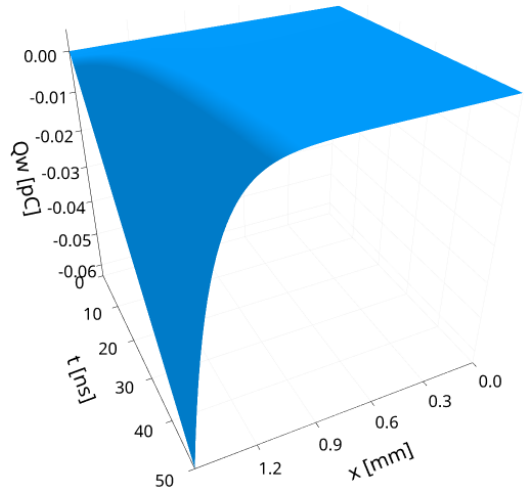

(c) 3D plot of $Q_w(x,t)$.

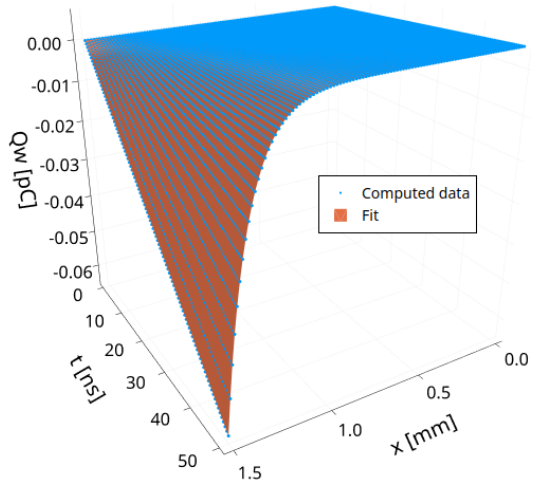

(d) Plot of $Q_w(x,t)$ fit. $\chi^2 = 2.66 \times 10^{-31}$.

Figure 2.3: Plots of $Q_w(x,t)$ calculated from values obtained using the iterative process.

constant x. It is linearly proportional to time, and as x is rising, the constant of proportionality is decreasing. On the other hand, in Figure 2.3b, the time is constant, and one can see that the value of $Q_w(x,t)$ is (presumably) exponentially decreasing from a constant value. One of the relations that satisfy such behaviour is

$$Q_w(x,t) = (a - be^{cx+d})t. \tag{2.8}$$

The fitted surface can be seen in Figure 2.3d, and the values of the parameters are in Table 2.1.

Parameter	Value
a	$1.015\,94(2) \times 10^{-7}\,\mathrm{A}$
b	$9.469\,57(8) \times 10^{-11}\,\mathrm{A}$
c	$9037.03(6)\,\mathrm{m}^{-1}$
d	$-3.972\,19(9)$

Table 2.1: Values of the fit parameters

Now, the fitted function can be used to calculate the maximum of SEY at any time and point in space by dividing the value of $Q_w(x,t)$ by the electron charge and rounding the number to the nearest integer. This gives the approximate number of electrons inside the channel wall. However, this approach does not work. By looking at the plot in Figure 2.4, one can see that at the beginning of the channel, the number of electrons is zero, and at some points, the number is even negative. It is expected for the number to be maximum at time zero and at the entrance of the channel because, at the beginning, the channel is in its non-saturated mode. This means that the walls should contain the maximum number of available electrons. The number should drop later, and zero charge could be expected at the end of the channel, as there is usually a huge number of highly energetic electrons which are trying to produce new secondaries. For this reason, this approach was not used in later simulations.

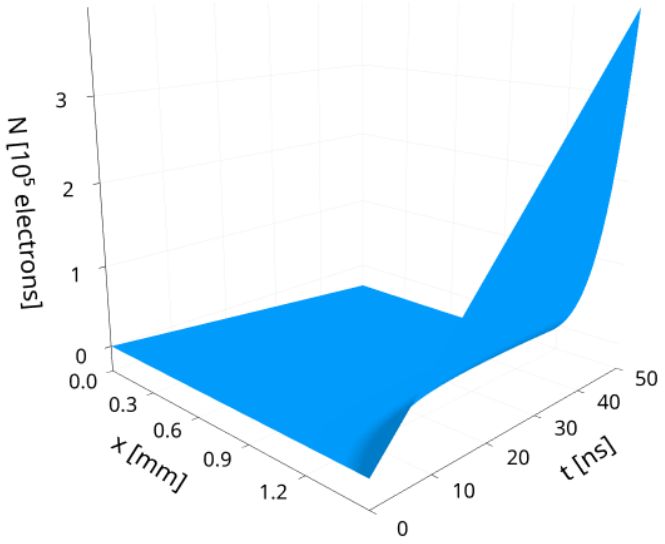

Figure 2.4: 3D plot of the number of electrons in the channel wall calculated by dividing (2.8) by electron charge.

2.3 Monte Carlo simulation

Monte Carlo simulation is a simulation that involves random sampling from some distribution. Randomness can be used to calculate a random or chaotic process or even for the numerical calculation of a deterministic problem. A typical example often described in the literature (for example [37]) is calculating π by randomly selecting points from a plane and checking if they belong to a unit disk.

The randomness involved in MCP simulations is mostly due to secondary electron emission. For example, the number of released particles and their initial velocities are randomly sampled from some distributions. Also, the position and velocity of the primary particle that entered the channel are usually random. Then, the movement of the particles is calculated from equations of motion, usually done by splitting time into discrete time steps and evolving the system in these steps. This approach is used to describe and simulate the microscopic aspects of a MCP-PMT.

The majority of MCP simulations done were Monte-Carlo simulations. This method was pioneered by Guest [5] in 1971. The Guest's model was a simple model that used random sampling from different distributions to obtain the number of released secondary electrons and their energies. The results of the simulation correspond well with the measured values. However, the simulation did not reproduce the saturation.

This work tried to develop a Monte Carlo simulation that would work in a similar fashion. Multiple distributions for the number of secondary particles were tested, along with different approaches for calculating the trajectories of the particles. Also, there was an attempt to optimize the simulations by reducing the number of spatial dimensions to 2D. In the end, two models that work fundamentally differently were tested. One exploits the fact that, in the simplest case, the electric field inside a microchannel is static in time and parallel to the channel axis. This means that the electrons' equations of motion can be solved analytically. In this thesis, the model is called the quasianalytical model. The name was chosen because it still uses randomness, and not every aspect of the simulation is analytical. The second model is based on the same principles as the original model developed by Guest. This thesis refers to this model as the PIC model. However, it should be noted that this model does not use all the techniques of the true PIC method. No field calculations were done during the simulations. Only the positions and velocities of particles were calculated.

2.3.1 Quasianalytical model

In the simplest case, the electric field inside a microchannel is stationary and parallel to the channel axis. This means that the equations of motion for the electrons can be derived and analytically solved. Then any quantity needed for the simulation can be easily calculated. Here is the analysis of the motion in 3D: imagine a channel of cylindrical shape of length L and radius R, which is oriented along the y axis. A bias voltage U across the channel generates an electrostatic field parallel to the channel axis but oriented in the opposite direction. The situation, along with the choice of the coordinate system, is pictured in Figure 2.5. The vector of the electrostatic field is

$$\vec{E} = -\frac{U}{L}\hat{y}, \tag{2.9}$$

where $\hat{y}$ is a unit vector oriented along the y axis. The typical value of the bias voltage is on the order of $10^3\,\mathrm{V}$, which means that the maximum energy of an electron in the channel is a few keV. The rest energy of an electron is $0.5\,\mathrm{MeV}$, which means that the non-relativistic theory can be safely used to derive the equation of motion. Because the electric field is stationary and homogenous, the

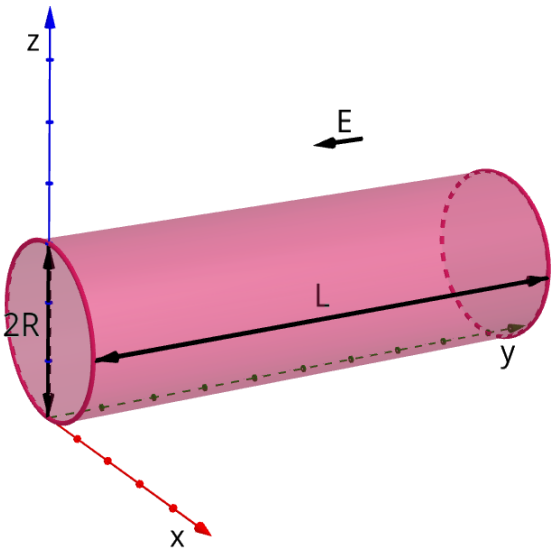

Figure 2.5: 3D drawing of the microchannel. Note that the y axis is shifted with respect to the channel axis.

problem is analogous to the motion of an object in a homogenous gravitational field, i.e. to free fall. This means that the equation of motion is

$$\vec{r} = \vec{v}_0 t + \frac{eU}{2mL} t^2 \hat{y}, \tag{2.10}$$

where m is electron mass and e is elementary charge. The electron charge is taken to be $-e$. The initial position is set to zero because only the movement of the electron between two collisions is of interest. Also, the time of travel between two collisions needs to be known. One can see from the equations that the x and z components of the electron velocity are constant in time and are equal to v_{0x} and v_{0z} respectively. This significantly simplifies the problem. Figure 2.6a shows

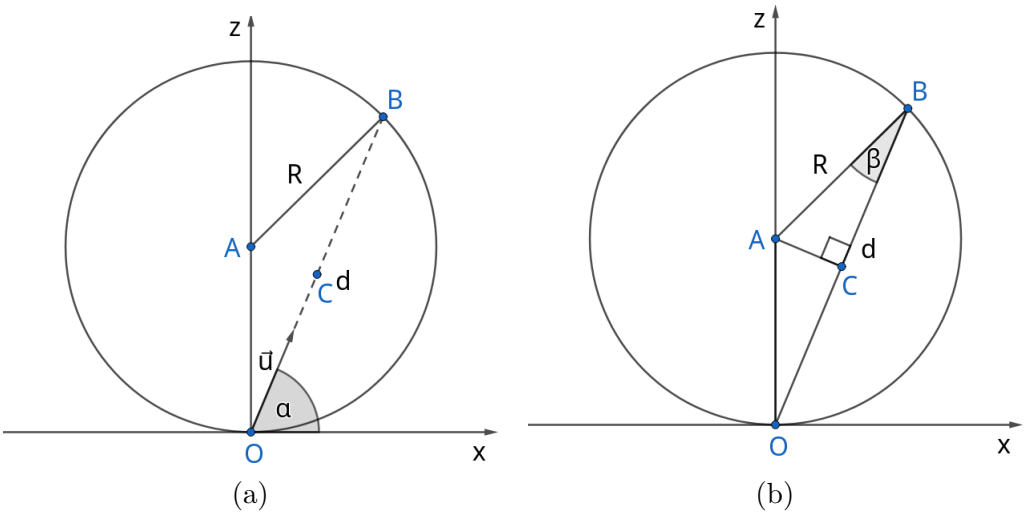

Figure 2.6: Drawings of the channel cross-section used for calculation of collision time. The vector $\vec{u}$ is the projection of $\vec{v}_0$ to xz plane. Point **A** is the center of the circle, point **B** is the collision point, and point **C** is auxilary point that splits the projection of the electron path d in half.

that the time needed for the electron to travel the distance d is the same as the collision time. The triangle OAB can be halved as on Figure 2.6b, and from the resulting right triangle ACB the distance d can be calculated using $\beta = \pi/2 - \alpha$

$$\cos\beta = \frac{d/2}{R} \tag{2.11}$$

$$d = 2R\cos\beta = 2R\sin\alpha. \tag{2.12}$$

The time of the collision is then

$$t_c = \frac{2R}{\sqrt{v_{0x}^2 + v_{0z}^2}}\sin\alpha. \tag{2.13}$$

Looking at the projection of $\vec{v}_0$ to xz plane, the angle α can be written using the components v_{0x} and v_{0z} as

$$\sin\alpha = \frac{v_{0z}}{\sqrt{v_{0x}^2 + v_{0z}^2},} \tag{2.14}$$

and from that the final expression for the collision time is

$$t_c = 2R\frac{v_{0z}}{v_{0x}^2 + v_{0z}^2}. \tag{2.15}$$

Now using equations (2.10) and (2.15) the collision energy E_c and the collision angle θ_c can be calculated. The collision energy is the electron's kinetic energy at time t_c. The collision angle is the angle between the velocity vector at time t_c and the surface normal $\hat{n}$ at the collision point. The velocity of the particle at the collision is

$$\vec{v_c} = \vec{v_0} + \frac{eU}{mL}t_c\hat{y}, \tag{2.16}$$

and the collision energy is then

$$E_c = \frac{1}{2}m\left(v_{0x}^2 + v_{0z}^2 + \left(v_{0y} + \frac{eU}{mL}t_c\right)^2\right). \tag{2.17}$$

Now the normal vector $\hat{n}$ needs to be found. It has to point towards the point $\mathbf{S} = (0, r_y(t_c), R)$, it starts at the collision point specified by $\vec{r}(t_c)$, and its magnitude is one. So it can be calculated as

$$\hat{n} = \frac{\mathbf{S} - \vec{r}(t_c)}{|\mathbf{S} - \vec{r}(t_c)|}. \tag{2.18}$$

Labeling the difference $\mathbf{S} - \vec{r}(t_c)$ as $\vec{n}$, it can be expressed as:

$$\vec{n} = (-r_x(t_c), 0, R - r_z(t_c)), \tag{2.19}$$

with magnitude

$$|\vec{n}| = \sqrt{r_x^2(t_c) + r_z^2(t_c) + R^2 - 2Rr_z(t_c)}. \tag{2.20}$$

Actually, from the definition of the vector $\vec{n}$, it should be obvious that its magnitude has to be equal to R, as it is a vector pointing from the edge to the centre of the cross-section circle. This means that the normal vector is

$$\hat{n} = \frac{1}{R}(-r_x(t_c), 0, R - r_z(t_c)). \tag{2.21}$$

This expression does not say much about $\hat{n}$, so let's replace $r_x(t_c)$ and $r_z(t_c)$ with their values. The equation (2.10) could be used, but the values $r_x(t_c)$ and $r_z(t_c)$ can be expressed using the angle α as

$$r_x(t_c) = 2R\sin\alpha\cos\alpha, \tag{2.22}$$

$$r_z(t_c) = 2R\sin^2\alpha. \tag{2.23}$$

This follows from the fact that in the projection to the xz plane, the collision point lies on the circle as in Figure 2.6a. In polar coordinates, the angle α is the polar angle of the projection, and d is its magnitude. Using equation (2.14) for the $\sin\alpha$ and a similar expression for $\cos\alpha$, where v_{0z} is replaced by v_{0x}, the final relation is

$$\hat{n} = \left(-2\frac{v_{0x}v_{0z}}{v_{0x}^2+v_{0z}^2}, 0, 1-2\frac{v_{0z}^2}{v_{0x}^2+v_{0z}^2}\right). \tag{2.24}$$

The collision angle θ_c can be calculated from the equation for the dot product of the normal vector $\hat{n}$ and the velocity vector at the collision time as

$$\theta_c = \arccos\frac{\vec{v}(t_c)\cdot\hat{n}}{|\vec{v}(t_c)|} \tag{2.25}$$

These calculations assume the electric field was parallel to the channel axis. Usually, the microchannels are not perpendicular to the face of an MCP, which means that the electric field is not parallel. Let's say that the electric field is at angle ϕ, so the vector of the field is

$$\vec{E} = -\frac{U}{L}(0, \cos\phi, \sin\phi). \tag{2.26}$$

In this case, the rotational symmetry is lost and the general equation

$$\vec{r} = \vec{r}_0 + \vec{v}_0 t + \frac{eU}{2mL}t^2(0, \cos\phi, \sin\phi). \tag{2.27}$$

has to be used, where $\vec{r}_0$ is the position of the electron at time zero. The trick used to find the collision time before cannot be used now, because the speed in the z direction is not constant. It has to be done by calculating the intersection of the trajectory (2.27) and the circle

$$x^2 + (z-R)^2 = R^2, \tag{2.28}$$

which is the perimeter of the cylinder. This means that the equation

$$(v_{0x}t_c + x_0)^2 + \left(v_{0z}t_c + \frac{eU}{2mL}t_c^2\sin\phi - R + z_0\right)^2 = R^2 \tag{2.29}$$

needs to be solved for t_c. After expansion equation 2.29 leads to a general quartic equation which can be solved either numerically or analytically. The analytical solution has an intricate structure, so software like Wolfram Mathematica [38] can be used to find the solution. Similarly, to the previous case, the collision energy is the kinetic energy at time t_c

$$E_c = \frac{1}{2}mv_c^2, \tag{2.30}$$

but in this case v_c has the form

$$\vec{v}_c = \vec{v}_0 + \frac{eU}{mL} t_c (0, \cos\phi, \sin\phi). \tag{2.31}$$

The expression (2.25) for the collision angle can also be used in this case, but the general formula (2.21) for the normal vector $\hat{n}$ has to be used instead of (2.24).

There was an attempt to develop a model that would work in the following way using the derived equations:

1. At the time zero, the primary electron is introduced into the microchannel. During the testing of the model, the electron appeared at point $(0, 0, 0)$, had random energy, and the direction of its velocity was also randomly sampled from a hemisphere pointing towards positive z and with the centre at the origin.

2. Using the equations, the trajectory of the primary electron to the collision point was calculated along with the collision time, energy, and angle.

3. Using the collision energy and angle, the SEY was estimated using a SEY function. This estimated value was then used as the mean value for the Poisson distribution, from which the final number of secondaries was randomly sampled.

4. From the collision point, new secondary electrons were introduced into the simulation. The energy of the primary electron was decreased by the energies of the secondaries. Then the process was repeated for every electron until they all left the channel.

The same function as Guest used in his original model was used for SEY. The function gives this relation between the secondary emission coefficient δ, the collision energy and the collision angle

$$\delta' = \left(E'_c \sqrt{\cos\theta_c} \right)^{\beta} \exp\left[\alpha(1 - \cos\theta_c) + \beta(1 - E'_c \sqrt{\cos\theta_c}) \right], \tag{2.32}$$

where $\delta' = \delta/\delta_m$ and $E'_c = E_c/E_{cm}$, where δ_m is the maximum of the secondary emission coefficient and E'_{cm} is the collision energy that corresponds to δ_m. The values of the collision energies used in this equation are in electronvolts. The constant α is related to the properties of the material from which the channel is made, and its value has to be determined experimentally. The constant β is determined by fitting known secondary emission curves at normal incidence. In Guest's model, two values of β were used, for $E'_c < 1$ the value was somewhere between 0.55 and 0.65, while for $E'_c \gg 1$ the value was chosen to be 0.25. In the original paper [5], the value of α was chosen to be 0.62. For the model to be comparable with Guest's model, the same values for the constants were used. Equation (2.32) provides the normalized value for the secondary emission coefficient. The values of δ_m and E_{cm} had to be determined. Adams and Manley [6] provide a simple model of MCP gain that involves calculating the collision energy and the secondary emission coefficient. In the paper [6], the maximum collision energy is determined to be

$$E_{cm} = \frac{U^2}{4E_0\alpha^2}, \tag{2.33}$$

where U is the bias voltage on the microchannel, E_0 is the initial energy of the electron in electronvolts, and α in this case is the length-to-diameter ratio. Then the secondary emission coefficient is said to be proportional to the collision energy with a proportionality constant K

$$\delta_m = KE_{cm}. \tag{2.34}$$

The same relation between δ and the collision energy in electronvolts also appear in [4] which helped to determine the value of the constant. The paper [4] says that the constant should be approximately equal to 0.2, which is the value used.

All the initial energies in the simulation were sampled from a Raylight distribution with the mean energy of 50 eV. Guest also used this distribution in his model. It is commonly used when a magnitude of a vector is randomly generated. This distribution naturally arises when a vector's components are uncorrelated and follow a normal distribution with the same variance and zero mean. The component of the velocity vectors was then generated in spherical coordinates, the azimuth angle ϕ was sampled from a uniform distribution with range $\phi \in [0, \pi]$, and the polar angle θ was sampled from a raised cosine distribution with mean $\mu = \pi/4$ and spread $s = \pi/4$. These values were used so the polar angle would fall into a range $\theta \in [0, \pi/2]$, as the raised cosine distribution is defined in the range $[\mu - s, \mu + s]$.

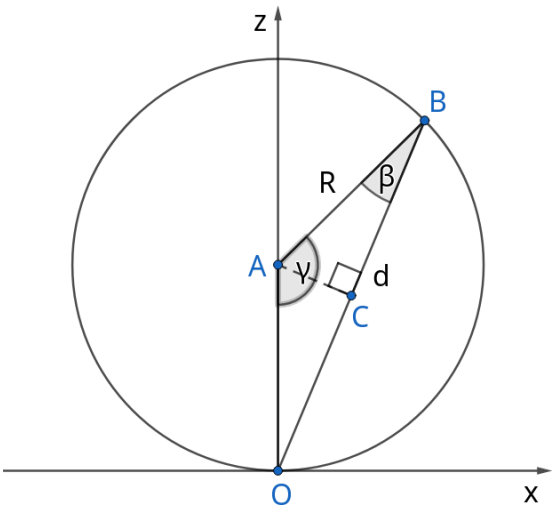

Figure 2.7: Drawing used for deriving the rotation angle γ. The triangle ACB from Figure 2.6b can be used to calculate the γ angle.

Looking at equation (2.10), one can see that the trajectory starts at point $(0, 0, 0)$. All the trajectories in this model are generated from this point, even if a new secondary electron appears further down the microchannel. This can be safely done because the problem has translational symmetry. However, when one wants to reconstruct the whole path of an electron from where it appeared to the end of the microchannel, the trajectories have to be stitched together. The subsequent trajectory has to start at the last collision point, but the "upward" direction for the last and the subsequent trajectory is different. The vector (2.10) of the subsequent trajectory needs to be rotated to point inside the microchannel. The rotation angle γ can be calculated from geometry in Figure 2.7. The point

at which the new trajectory has to start is the point **B**. From the triangle ACB the sine of $\gamma/2$ is

$$\sin\frac{\gamma}{2} = \frac{d}{2R}, \tag{2.35}$$

substituting (2.12) for d the equation transforms to

$$\sin\frac{\gamma}{2} = \sin\alpha, \tag{2.36}$$

from which follows that

$$\gamma = 2\alpha. \tag{2.37}$$

This also follows from the fact that the sum of the angles inside a triangle is equal to π, which means that $\gamma/2 = \pi - \pi/2 - \beta$. Also, it was shown that $\beta = \pi/2 - \alpha$, so $\gamma/2 = \pi - \pi/2 - \pi/2 + \alpha$ and equation (2.37) is recovered. Now substituting α from equation (2.14) the expression for gamma is

$$\gamma = 2\arcsin\frac{v_{0z}}{\sqrt{v_{0x}^2 + v_{0z}^2}} \tag{2.38}$$

This is not the full answer, as this angle would work only for collision points with a positive or zero x component. In the other case, the next trajectory has to be rotated by angle $-\gamma$. So the next trajectory is rotated around the y axis using the rotation matrix

$$\overline{M} = \begin{pmatrix} \cos(\gamma) & 0 & \operatorname{sgn}(B_x)\sin(\gamma) \\ 0 & 1 & 0 \\ -\operatorname{sgn}(B_x)\sin(-B_x\gamma) & 0 & \cos(\gamma) \end{pmatrix}, \tag{2.39}$$

where B_x is the x component of the collision point, and

$$\operatorname{sgn}(x) = \begin{cases} -1 & x < 0 \\ 0 & x = 0 \\ 1 & x > 0 \end{cases} \tag{2.40}$$

2.3.2 PIC model

The equations derived in the previous section work only in the simplest case when the interactions between the electrons are neglected. This approach also does not work if one wants to study the effects of the fringe fields. In such cases, one has to resort to solving the trajectories numerically. This is usually done by dividing the time into discrete time steps and calculating all the positions, velocities, and other quantities only in these steps. The interval Δt between two time steps is usually chosen to be constant, so the next $k+1$ time step is calculated as $t_{k+1} = t_k + \Delta t$. The code responsible for calculating the trajectories is in literature often called a particle mover [39]. It implements some method to calculate the positions and velocities. The two most popular are the Leap frog and Boris method [39]. Both methods calculate the velocity between two time steps and then calculate the new position from the velocity. The general equations of the Leap frog method for the movement of particles in an electromagnetic field are

$$\vec{v}_{k+1/2} = \vec{v}_{k-1/2} + \frac{e}{m}\left(\vec{E}_k + \frac{\vec{v}_{k+1/2} + \vec{v}_{k-1/2}}{2} \times \vec{B}_k\right)\Delta t, \tag{2.41}$$

$$\vec{x}_{k+1} = \vec{x}_k + \vec{v}_{k+1/2}\Delta t. \tag{2.42}$$

From the equations, one can see that it is a straightforward method. The new velocity is calculated from its old value, and the acceleration simply by multiplying the acceleration with some short time Δt and adding the value to the old velocity value. This is nothing more than just a simple numerical integration. The new position vector is calculated from the velocity in the same manner. The Boris method can look more complicated at first sight. The equations are:

$$\vec{x}_{k+1} = \vec{x}_k + \vec{v}_{k+1/2}\Delta t, \tag{2.43}$$

$$\vec{v}_{k+1/2} = \vec{u}_+ + q\vec{E}_k, \tag{2.44}$$

$$\vec{u}_+ = \vec{u}_- + \left(\vec{u}_- + \left(\vec{u}_- \times \vec{h}\right)\right) \times \vec{s}, \tag{2.45}$$

$$\vec{u}_- = \vec{v}_{k-1/2} + q\vec{E}_k, \tag{2.46}$$

$$\tag{2.47}$$

where the values of $\vec{h}$, $\vec{s}$ and q are:

$$\vec{h} = q\vec{B}_k, \tag{2.48}$$

$$\vec{s} = 2\frac{\vec{h}}{1+h^2}, \tag{2.49}$$

$$q = \frac{e\Delta t}{2m}. \tag{2.50}$$

This method looks substantially more complicated, but its advantage is that it require fewer operations which means less CPU time. In this form, the Boris method requires 39 operations: 18 additions and 21 multiplications. In special cases when $\vec{B}$ has one or two zero components, the number of operations can be reduced to 17. However, there is no magnetic field in the simulations. In such a case, the Boris method is reduced back to the Leap frog method. With $\vec{B} = \vec{0}$ equations (2.48) and (2.49) are zero, and $\vec{u}_+$ is equal to $\vec{u}_-$. By substituting (2.46) and (2.50) into (2.44) the equation (2.41) for the case of zero magnetic field is recovered.

The algorithm of the PIC simulation is similar to the algorithm of the quasianalytical simulation. The only difference is in the way of calculating the trajectories. The quasianalytical simulation loops over the electrons inside the channel until all electrons leave the channel. During this process, it assigns the analytically calculated trajectories to electrons. The PIC simulation also loops over electrons but does it every time step. During the time step, the positions of all electrons in the channel are advanced using the Leap Frog algorithm. After adjusting the positions, the simulation checks if any collision occurred using the condition

$$r_x(t)^2 + (r_z(t) - R)^2 \geq R^2, \tag{2.51}$$

where $r_x(t)$, and $r_z(t)$ are the x and z coordinates of electron poistion at time t. If condition (2.51) is true, a collision occured and new secondary electrons are introduced in the same way as in the quasianalytical simulation.

2.3.3 Results

In this section, the results from testing of the Monte Carlo simulations are presented. A comparison between a simulation in two spatial dimensions and a

simulation in three spatial dimensions was performed. The 2D simulation was based on the simulation done by Guest [5], and the 3D simulation was calculated by the quasianalytical simulation. In both cases the bias voltage was set to 2 kV, the length of the microchannel was 1.5 mm, and the radius was 10 µm. In Figure 2.8, the histograms of the number of collisions are plotted. The data

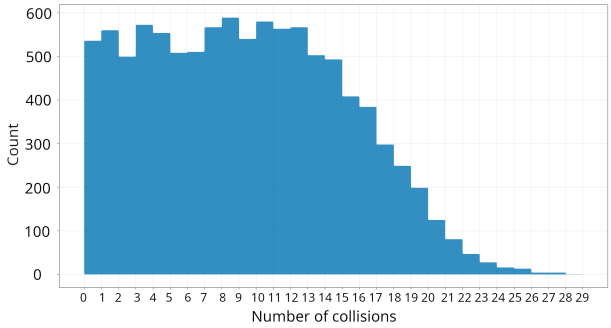

(a) For 2D simulation.

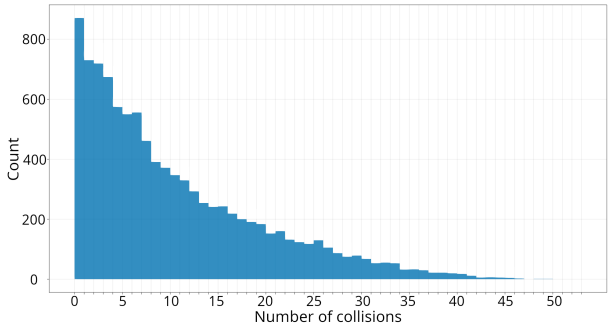

(b) For 3D simulation.

Figure 2.8: Histograms of the total number of collisions that occured during one run of the simulation. The quasianalytical simulation was used to obtain the histograms.

were generated by repeatedly propagating an electron from one end of the microchannel to the other. For each simulation, a one thousand such propagations were made. The most obvious is the difference in the shapes of the histograms. There is also a substantial difference in the maximum number of collisions. In the case of the 2D simulation, 29 collisions occurred during one simulation at maximum, while for the 3D simulation, this number was 53. In both cases, there were simulations in which no collisions occurred, and the electron passed through the microchannel. For the 3D simulation, the single collision simulations were most likely, while for the 2D simulation, the histogram is more or less flat until the number 14, when the histogram starts rapidly decreasing. The difference between the maximum number of collisions can be explained by the geometry. In the 2D case, the electron can travel only up, down and forward and collide only with the upper or lower wall. In the 3D case, the electron can also travel to the sides, and the wall surface is much bigger, significantly improving the chance of a collision.

In Figure 2.9, there are histograms of energy the electrons had when they left the microchannel. The general shape of the histograms is similar, but the mean energy is different. For the 2D case, the mean energy is 14.18 eV, while for the 3D case the mean energy is 31.81 eV. Again, the difference can be explained by the geometry of the microchannels. Figure 2.10 shows the typical energy distribution

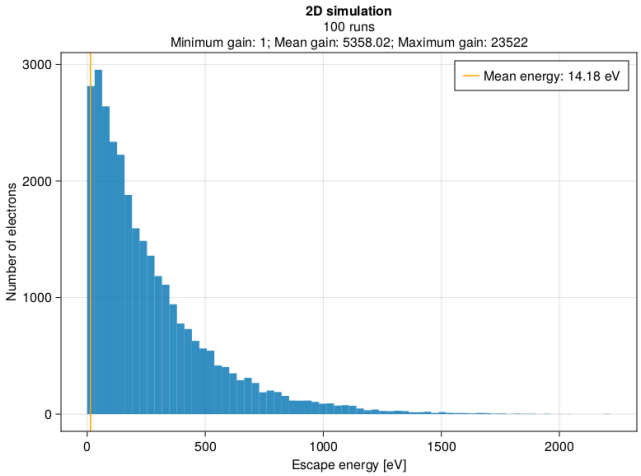

(a) For 2D simulation.

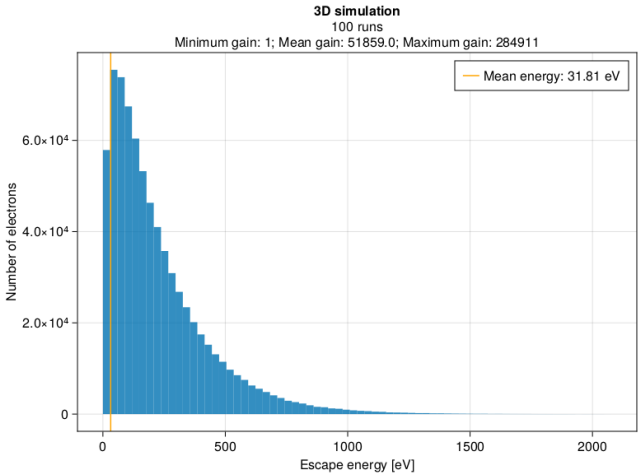

(b) For 3D simulation.

Figure 2.9: Simulated energy distribution of the output electrons. The distributions were obtained using the quasianalytical simulation.

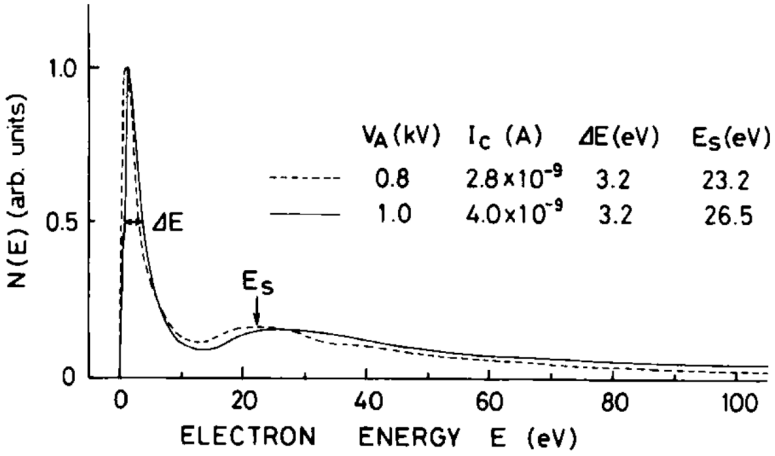

Figure 2.10: Measured energy distribution of output electrons of unsaturated MCP [40].

of output electrons for an unsaturated MCP. According to the plot, the majority of the electrons have small energies $\sim 1.6\,\mathrm{eV}$. From this value, the distribution quickly diminishes. The distribution has a small peak at energy $\sim 25\,\mathrm{eV}$ and then slowly goes to zero. The distributions from Figure 2.9 show different behaviour. The maxima of the distributions are ten times higher. The shapes of the distributions show a decrease similar to the first peak in Figure 2.10, however the decrease is much slower. The distributions from the simulations show a significant number of electrons with energies higher than $100\,\mathrm{eV}$. The small energies of the typical distribution suggests that the output electrons did not have enough time to gain energy, which means that the electrons were either released near the end of the channel or they encountered a collision near the end. As is shown later in the text, the electrons in the quasianalytical simulation can travel significant distances and gain a lot of energy, which can explain the differences in the distributions. However, the quasianalytical simulation does not consider the effects of fringe fields and the electric field in the simulation is parallel to the channel axis, which also influences the energies.

Figure 2.11 is the comparison of trajectories produced by the quasianalytical simulation and the PIC simulation. As one can see, the trajectories are substan-

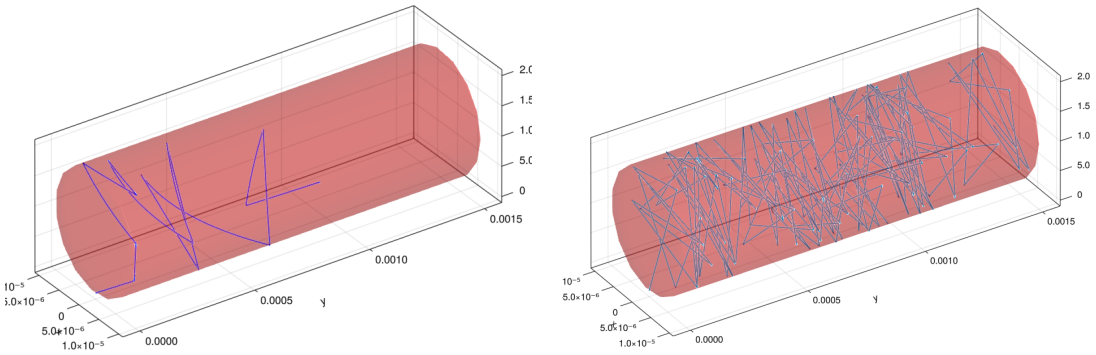

(a) Trajectory produced by the quasianalytical simulation.

(b) Trajectory prodeced by the PIC simulation.

Figure 2.11: Comparison of trajectories produced by the quasianalytical simulation and the PIC simulation. The red opaque cylider represent the microchannel.

tially different. The quasianalytical simulation produced long trajectories, and it is easy to see the curvature of the parabolas. The PIC simulation produced short trajectories. They look mostly straight, but a closer look reveals the curvature. Near the point $y = 0.0015\,\mathrm{mm}$ in Figure 2.11b, there is one longer trajectory. Such trajectories were sometimes produced during the testing, and they split the channel into two or three sections. In the sections, the trajectories were short, and a long trajectory separated them. The mechanism of the secondary emission probably caused the difference between the length of the trajectories. The comparisons of the 2D and the 3D simulation were made using the mechanism described in the section 2.3.1, but the trajectories in Figure 2.11a were plotted using the Furman-Pivi model of secondary emission. This means that the electrons had different energies after collisions. Using the Furman-Pivi model, the absorption of the electrons by the channel wall can be simulated, and that is the reason why the trajectory in Figure 2.11a ends before the end of the microchannel. The difference between the lengths of the trajectories has an obvious effect

on the secondary emission and the gain. Longer trajectories mean fewer collisions, producing a smaller number of secondary electrons. This leads to smaller gain. On the other hand, the longer trajectories should be responsible for higher electron energies, resulting in more secondary electrons produced in one collision.

The performance of the simulations was also tested. Both the quasianalytical simulation and the PIC simulation were written in Julia programming language [41]. There exists a Julia package called BenchmarkTools.jl [42] that simplifies the benchmarking process. This package was also used to test the simulations. To test the performance, a single electron was repeatedly propagated through the microchannel, and the computation time was measured along with the memory allocations. The results are in Table 2.2. The tests were performed on a laptop

	Quasianalytical simulation	PIC simulation
Number of samples	10000	41
Min. time	12.142 µs	92.471 ms
Max. time	20.168 ms	158.499 ms
Median time	192.804 µs	120.651 ms
Mean time	268.726 µs	122.238 ms
Allocated memory	3.98 KiB	73.35 MiB

Table 2.2: Result of performance tests of the simulations.

with 8 GB of RAM and Intel® Core™ i5 processor of 8th generation with four cores and Hyper-Threading enabled. As expected, the quasianalytical simulation is faster and requires substantially less memory. This makes sense because the quasianalytical simulation needs to perform fewer calculations. The problem is solved beforehand, and the required quantities are calculated directly from generated values. On the other hand, the PIC simulation has to calculate the velocity and the position of the particle repeatedly at every time step. This requires much more computation. The PIC simulation also requires more memory because the velocity and position of particles are saved to memory in each time step. The quasianalytical simulation saves only the initial values and the calculated collision time, energy and angle. Also, the values are stored only if a collision occurs.

The simulations were mostly tested and used only with few electrons. They were also tested without any constraints on the number of electrons but such runs never finished, even after multiple hours of running. Some runs ran for more than a day before being stopped. This is a problem with both simulations. An attempt was made to improve the situation. The biggest problem is the amount of generated data. The so-called *producer-consumer* approach was tested. Using this approach, the simulations were split into two threads; one thread computed the simulation and generated the data, while the second thread wrote the data to disk. Using an appropriate CPU with at least two cores, the threads can run almost independently. This way, the simulation can run without the overhead of writing the data to the disk and without the need to store all the data in RAM. Unfortunately, this approach did not resolve the problem. Later it was found that the problem was caused by the way Julia manages the memory. As the performance test showed, both simulations allocate memory while they are running, and this memory has to be deallocated when it is no longer needed. Julia uses a garbage collector to do this. This approach means that the programmer

does not have to free the memory manually. It was found that while the garbage collector is running, both threads are paused and resumed later. It was also found that because of how the simulations are written, the garbage collector is executed often. This significantly slowed down the simulations. The problem can be resolved by rewriting the simulations in a more appropriate language like C or C++. Unfortunately, it was not done in this work due to the shortness of time, and other approaches to simulations were explored. Namely the use of COMSOL Multiphysics® was tested.

2.4 COMSOL Multiphysics®

2.4.1 Overview

COMSOL Multiphysics® [43] is a commercial simulation software capable of simulating a wide variety of physical phenomena. For example, it can simulate problems involving heat transfer, fluid dynamics, material stress, and more. The exhaustive list is accessible on [44]. The software can also simulate electromagnetic fields and the motion of charged particles in the fields. The particles can interact with each other and with the fields and modify them. This software is known to the scientific community, and it was already used for studying electric fields inside MCP microchannels [10, 45, 46]. Some advantages of COMSOL® include:

- Easy to use graphical interface, a screenshot of which is shown in Figure 2.12
- Multi-platform support: it can run on Linux, Windows and Mac OS
- Simulations can be calculated on a cluster
- Definition of the model geometry can be done inside the software
- Connection to MATLAB® via LiveLink™
- Execution of custom C/C++ code

Figure 2.12 shows the user interface of COMSOL Multiphysics® running on Linux operating system.

2.4.2 Model definition

The easiest way to define a model is to use the *Model Wizard*, which is a tool that helps with the basic definitions, like the number of spatial dimensions, the physics that one wants to study and how. For this model the 3D option was selected (Figure 2.13), and it is supposed to simulate the motion of electrons, so the *Charged Particle Tracing* module was added (Figure 2.14).

The model is designed to simulate the evolution over time, for which the *Time Dependent* study was used (Figure 2.15). After finishing the steps of the *Model Wizard*, one can see all the definitions in a tree-like view under the *Model Builder* tab, which is used to add and remove definitions.

In the next step, model geometry is defined. In the simplest case, the model simulates the behaviour of a single microchannel, so a cylinder was used as a

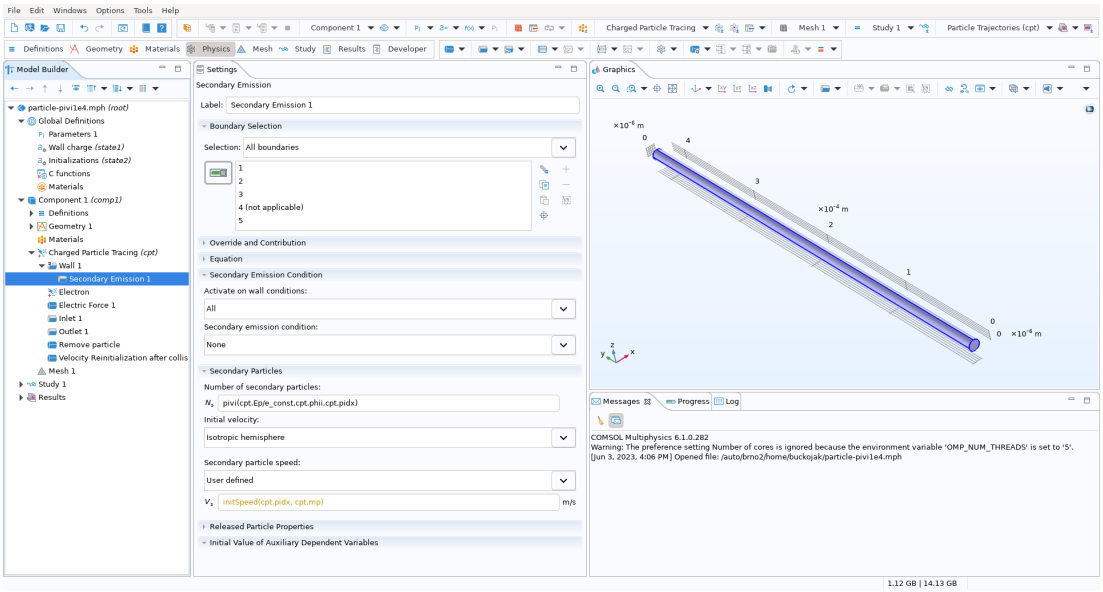

Figure 2.12: Screenshot of COMSOL Multiphysics® user interface on Linux. On the left side there is the tree view of the model definitions followed by the settings view. On the right the 3D view of the geometry is placed. Under it is a pane with messages and progress indicator. On the top of the window is a toolbar from which varios modifications to the model can be made.

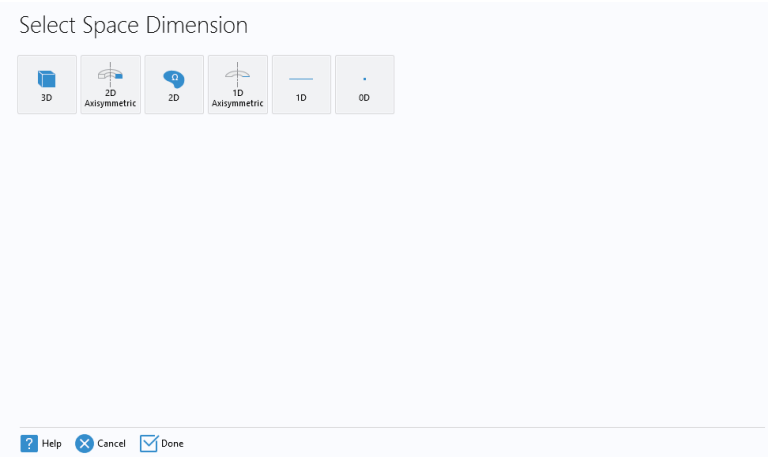

Figure 2.13: Selection of number of spatial dimensions in the *Model Wizard*. The 3D option was selected.

simulation domain. The length and radius of the cylinder could be set to a fixed number, but COMSOL® allow to define parameters. They can be easily adjusted in the future. The main characteristics of a microchannel are diameter and length-to-diameter ratio, so such parameters were defined. Then, a *Wall* node was defined and linked to the geometry. This node defines what should happen when a particle hits the wall. There are multiple options like *Stick, Disappear*, and *Pass through*, which cause the particles to stick to the wall, disappear from the simulation or pass through the wall, respectively. There is also the option of *Isotropic scattering*, which was used. Next, the type of particles in the simulation were defined by adding the *Particle properties* node; COMSOL® offers a variety of predefined properties, including electrons. An electric force was added into the

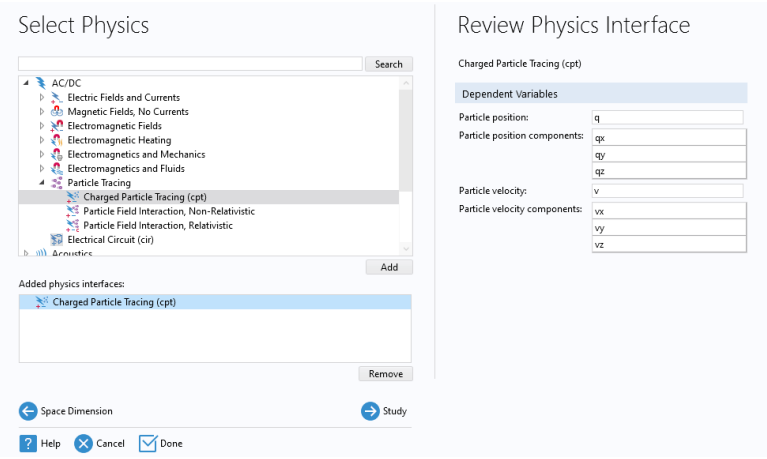

Figure 2.14: Selection of physics to simulate in the *Model Wizard*.

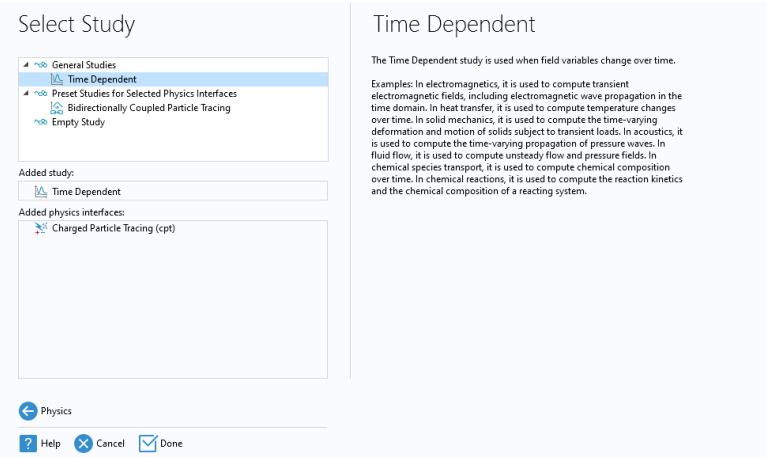

Figure 2.15: Selection of so-called study in the *Model Wizard*. The study describes if one wants to know how the system is evolving in time, or there is a stationary study which is used to solve systems independend of time. These two are not the only studies one can choose.

model using the *Electric force* node. The electric field was defined as a vector $(0, -U/len, 0)$, where U and len are parameters of bias voltage and length of the microchannel. To introduce electrons into the simulation, an *Inlet* node was added and set to release one electron at the initial time at a random position at the end of the microchannel. The initial velocity vector of the initial electron was set to have a random direction and magnitude of $v0$, which is another parameter. All defined parameters are in Figure 2.16. At the end of the microchannel, the electrons should leave the microchannel, so an *Outlet* node was added. This node defines what should happen to electrons which reach the wall at the end of the microchannel. The node offers two options: *Freeze* and *Disappear*, and the second one was used. In Figure 2.17, one can see all the definitions. The rest of the nodes not mentioned yet are described later in the text.

Parameters

Label: Parameters 1

Parameters

Name	Expression	Value	Description
diam	10[um]	1E-5 m	Diameter of the micro-channel
a	42	42	Length-to-diameter ratio
T0	1[keV]	1.6022E-16 J	The initial energy of primary electron
v0	sqrt(2*T0/(me_const))	1.8755E7 m/s	The initial speed calculated from T0
len	a*diam	4.2E-4 m	Length of the micro-channel
U	2.4[kV]	2400 V	Bias voltage
maxSecondaries	10	10	Maximum number of secondary particles
electrodeDistance	1e-4[m]	1E-4 m	Distance between an electode and channel openenig

Figure 2.16: Parameters used in the COMSOL® model.

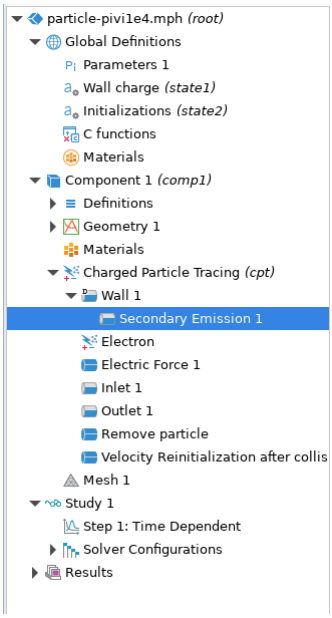

Figure 2.17: All definitions used in the COMSOL® model.

2.4.3 Implementation of the Furman-Pivi model

The model developed by Furman and Pivi [16] is quite complex; it contains multiple probability distributions from which the values are randomly sampled and a substantial amount of parameters. Because of this, adding the model into the COMSOL® simulation is not straightforward. There are two options for how to do it. The first one is to implement it in MATLAB® and then use the LiveLink™ connection. The second option is to write a C/C++ dynamic library and load it into COMSOL®. In this work, the second option was used for multiple reasons. MATLAB® is yet another commercial software that requires its separate license. Also, the ability to use LiveLink™ with COMSOL® is not included in all COMSOL® licenses. Finally, the MATLAB® code would be executed in a separate process and the communication between COMSOL® and MATLAB® would have to be done via some interprocess communication (IPC). This is generally slower than loading a dynamic library into a program and running the code directly.

The disadvantage of using the dynamic library is the possible non-portability of the written C/C++ code, the final implementation was written and tested only on a Linux operating system.

The library is used inside the model in the following way. Firstly the library is included in the model by adding *External* node into the definitions. In the model, the node is renamed to *C functions*. In the settings for the node, the path to the library file is supplied, and a list of functions evaluated by the library and their arguments are defined. Under *Advanced* tab, one can specify initialization data, but unfortunately parameters cannot be passed to the library this way. The value of the initialization data field is passed directly to the `init` function of the library as a string. In the model, it is used to pass the path to a file with parameters needed by the Furman-Pivi model. The functions defined here can be used anywhere in the model; COMSOL® evaluates them by calling the `eval` C function exported by the library.

The library can evaluate the following functions:

- `pivi(Ek, theta, pidx)`: This function is evaluated when a particle hits the wall. It takes the particle's kinetic energy, collision angle, and particle index as arguments. This is the main function which calculates the number of secondary electrons and their energies. It returns the number of secondary electrons and saves the energies to an array. It also marks the primary particle for removal if no secondaries were produced or generates a new velocity vector for the primary particle and marks it for reinitialization.

- `initSpeed(pidx, mass)`: This function is evaluated when a secondary particle is introduced to the simulation. It takes the particle index and its mass as arguments. This function reads from memory the saved energy generated by the `pivi` function and returns the calculated speed. This value is then assigned by COMSOL® as the initial speed of the new particle.

- `shouldBeRemoved(pidx)`: This function is evaluated every time step. It takes the index of a particle on which the function is evaluated as an argument and returns the number one if the particle was marked by `pivi` function for removal, or zero otherwise.

- `shouldBeReinitialized(pidx)`: This function is evaluated every time step. It takes the index of a particle as an argument and returns the number one if the particle was marked by `pivi` function for reinitialization, or zero otherwise.

- `reinitializeVelocity(pidx, mass, component)`: This function is evaluated when a particle is reinitialized. It takes the particle's index, its mass, and the component of the new velocity vector as arguments and returns the value of the velocity component. The components are marked by numbers: x component is number one, y component is number two, and the z component is number three.

- `initPiviArrays(maxParticles)`: This function is evaluated at the start of the simulation. It takes the maximum number of secondary particles as an argument. It is used to initialize the auxiliary arrays inside the library.

This should be done inside the `init` C function, but the parameters cannot be passed into it, so this non-standard method had to be used.

A *Secondary emission* node was added to the *Wall* node to include secondary emission in the model. The setting for the *Secondary emission* node contains a variety of options, from which the most interesting are options for the initial velocity and the number of secondary particles. The reference to the `pivi` function was put into the field for the number of secondary particles, and for the initial velocity, the *Isotropic hemisphere* option was chosen. The initial speed was defined using the *User defined* option and the reference to the `initSpeed` function was put into the corresponding field.

Also, COMSOL® needs to reinitialize or remove the particles after a collision. Two *Velocity reinitialization* nodes were added to the model to do this. One of them was renamed to *Remove particle* and the second one to *Velocity reinitialization after collision*. In the settings for the *Remove particle*, the effect was set to *Disappear*, and the reference to the `shouldBeRemoved` function was used as the condition for the effect. For the second node, the `shouldBeReinitialized` function was used as the condition, and the effect was set to *reinitialize*. Then the new velocity components were set using the `reinitializeVelocity` function.

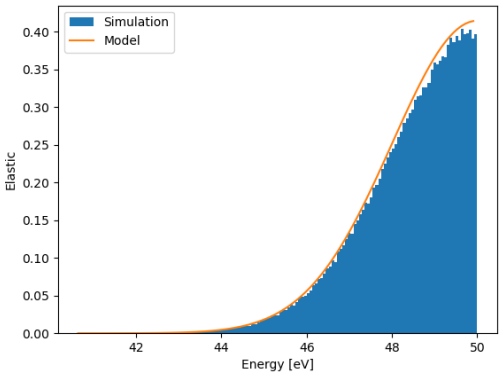

(a) Distrubution of the elastically scattered electrons.

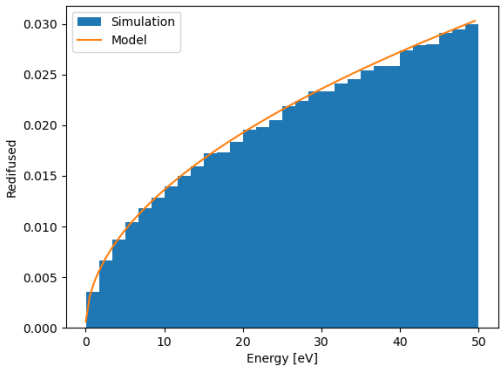

(b) Distrubution of the redifused electrons.

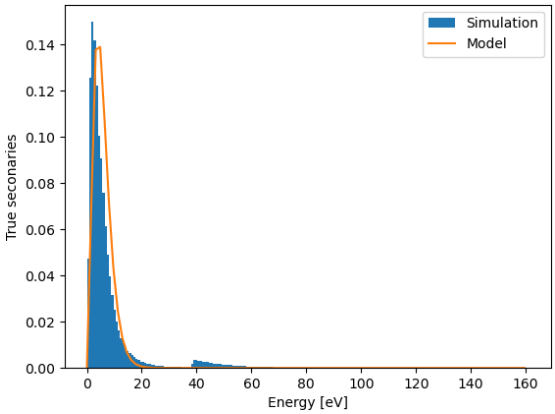

(c) Distrubution of the true secondaries.

Figure 2.18: Normalized energy distributions of secondary electrons for normal incidence and collision energy of 50 eV.

2.4.4 Validation of the implementation

The implementation of the Furman-Pivi model for secondary electron emission used in the COMSOL® model is based on the implementation done for PyECLOUD simulation code [17]. The authors of PyECLOUD also provide a simple test to validate the implementation. It consists of comparing histograms of energies provided by the algorithm with the theoretical PDFs. In Figure 2.18, one can see the result of the test for the implementation used in the COMSOL® model. One can see that for elastically scattered and rediffused electrons, the theoretical curves correspond well with the histograms calculated by the algorithm. For true secondaries, there is a small peak at the energy around 40 eV, which should not be there. The theoretical curve is almost zero in this region. However, this peak is small compared to the main peak at low energies, so it should not influence the results significantly. The theoretical curve is slightly shifted towards higher energies, this is because the mean for the theoretical curve is calculated from the simulated distribution, and the small peak pushes the mean to higher energy. However, the shape of the main peak matches the theoretical shape well, so this implementation can be considered to be valid. In the future, the problem with the small peak should be corrected if possible to obtain the most trustworthy results.

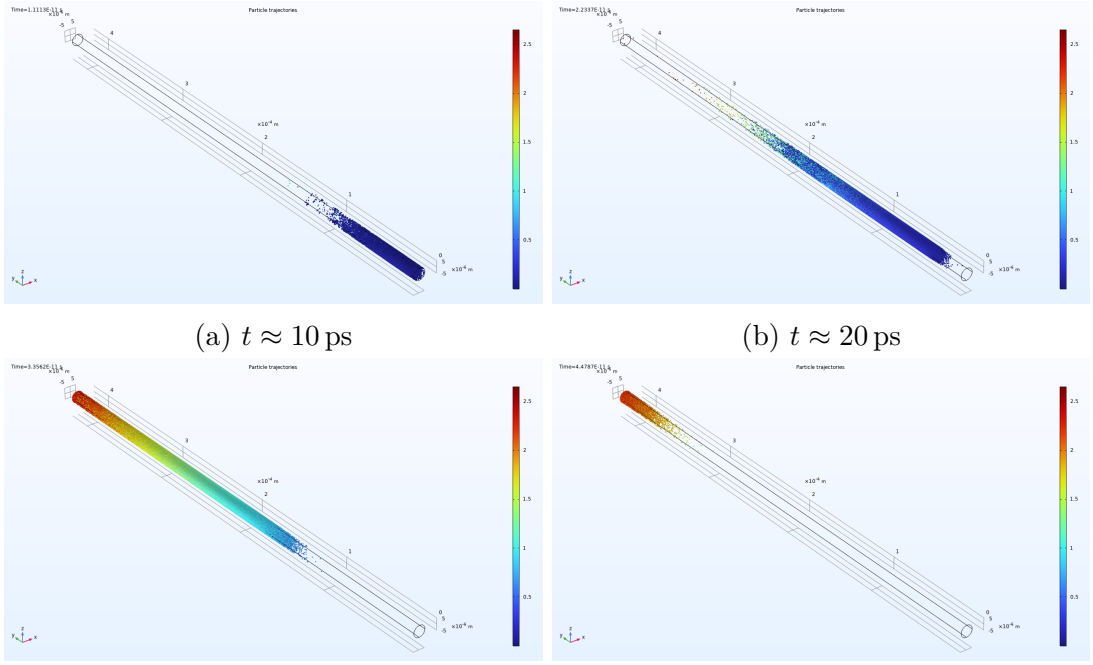

(a) $t \approx 10\,\mathrm{ps}$ (b) $t \approx 20\,\mathrm{ps}$

(c) $t \approx 30\,\mathrm{ps}$ (d) $t \approx 40\,\mathrm{ps}$

Figure 2.19: Positions of electrons inside the microchannel at different times. The colouring represents the speed of the electrons. Result from a test run using simplified secondary emission model. The colour axis is in $10^7\,\mathrm{m\,s^{-1}}$, the maximum value is $2.5 \times 10^7\,\mathrm{m\,s^{-1}}$, the middle value is $1.5 \times 10^7\,\mathrm{m\,s^{-1}}$.

2.4.5 Results

In this section, the results of the COMSOL® model are presented. The diameter of the microchannel was set to 10 µm and the length-to-diameter ratio was set to 42, which means that the length of the microchannel was 420 µm. Two configurations of the electric field were tested. The field was either parallel to the channel axis or it was tilted by 15°.

In Figure 2.19, the positions of electrons inside the microchannel are plotted. The first plot is the situation at time zero, and the time between subsequent plots is $\sim 10\,\mathrm{ps}$. These plots were made using a simplified model that did not use the Furman-Pivi model of secondary emission. The number of secondary electrons and the initial velocity of secondary particles were set to a fixed number. This was used to verify that the basic definitions of the COMSOL® model work. In this case, the propagation of the signal is clearly visible. The maximum speed reached was $\sim 2.5 \times 10^7\,\mathrm{m\,s^{-1}}$, and the transit time was $\sim 42\,\mathrm{ps}$, which is around ten times shorter than the typical transit time for MCP-PMT. This is not surprising because only a single microchannel was simulated, and most MCP-PMTs contain at least two MCPs in series. Also, the propagation of electrons from the photocathode and from MCP to the collector anode was not simulated. However, in this run, the transit time is not important. The fact that propagation and the multiplication of electrons occurred means that the model is configured properly.

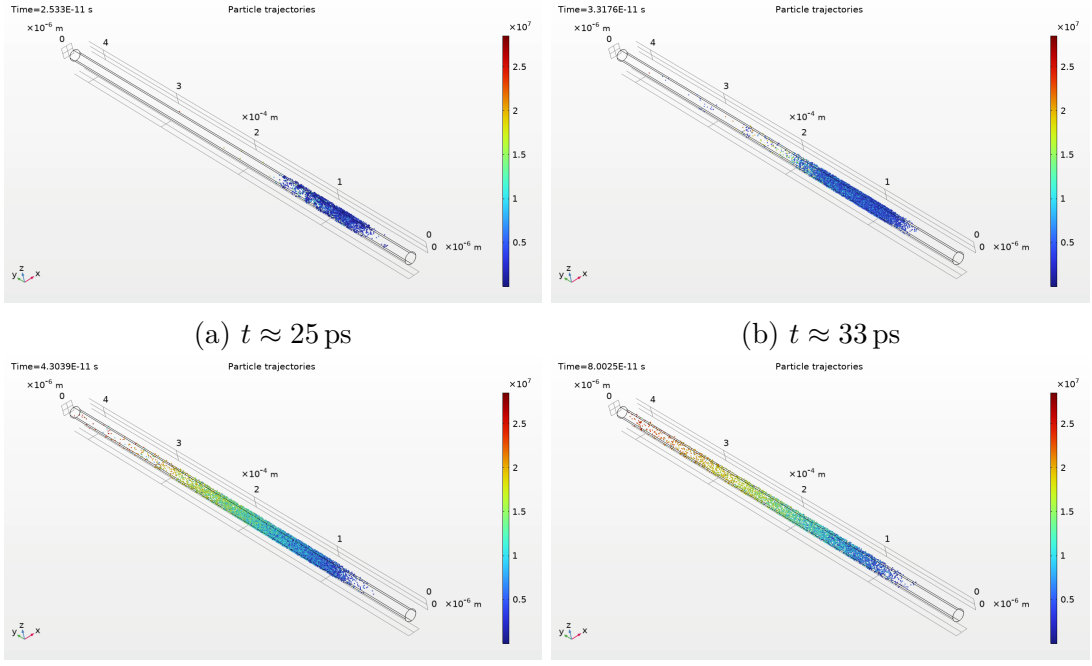

(a) $t \approx 25\,\mathrm{ps}$ (b) $t \approx 33\,\mathrm{ps}$

(c) $t \approx 43\,\mathrm{ps}$ (d) $t \approx 80\,\mathrm{ps}$

Figure 2.20: Positions of electrons inside the microchannel at different times. The colouring represents the speed of the electrons. The Furman-Pivi model of secondary emission was used. The colour axis is in $10^7\,\mathrm{m\,s^{-1}}$, the maximum value is $2.5 \times 10^7\,\mathrm{m\,s^{-1}}$, the middle value is $1.5 \times 10^7\,\mathrm{m\,s^{-1}}$.

Figure 2.20 shows the positions of electrons in the main COMSOL® model that is using the Furman-Pivi model for secondary emission. The maximum number of secondary particles was set to 10^4, and the electric field was set to be

parallel to the channel axis. The evolution of the positions in time is troubling in this case. The amplification of the signal can be clearly seen, but the signal spreads significantly, and the output pulse is deformed. This can also be seen in Figure 2.21, where histograms of the number of particles are plotted at different times. The creation of the pulse can be clearly seen, however the peak does not propagate to the end, but it spreads out and slowly disappears. The peak reaches the maximum height at the time $\sim$ 30 ps, because at that time, the maximum number of particles that can be in the simulation was reached. From the plots and animation of Figure 2.20, it looks like the particles are trapped inside the microchannel. This behaviour is unexpected because there is a strong electric field acting on the particles that should accelerate them towards the end of the microchannel. This means that there is a problem with the COMSOL® model. The run without the Furman-Pivi model showed good propagation of the signal, which means that the problem could be in the implementation of the secondary emission. The trapping of the particles could be caused by the *Velocity reinitialization* that should give particles new velocity after they collide with the wall. Another reason could be the numerical method used by COMSOL® to calculate the positions. This can be configured, and a user can select between multiple numerical methods and configure time steps and other parameters of the methods. Multiple configurations were tested, but none of them improved the behaviour.

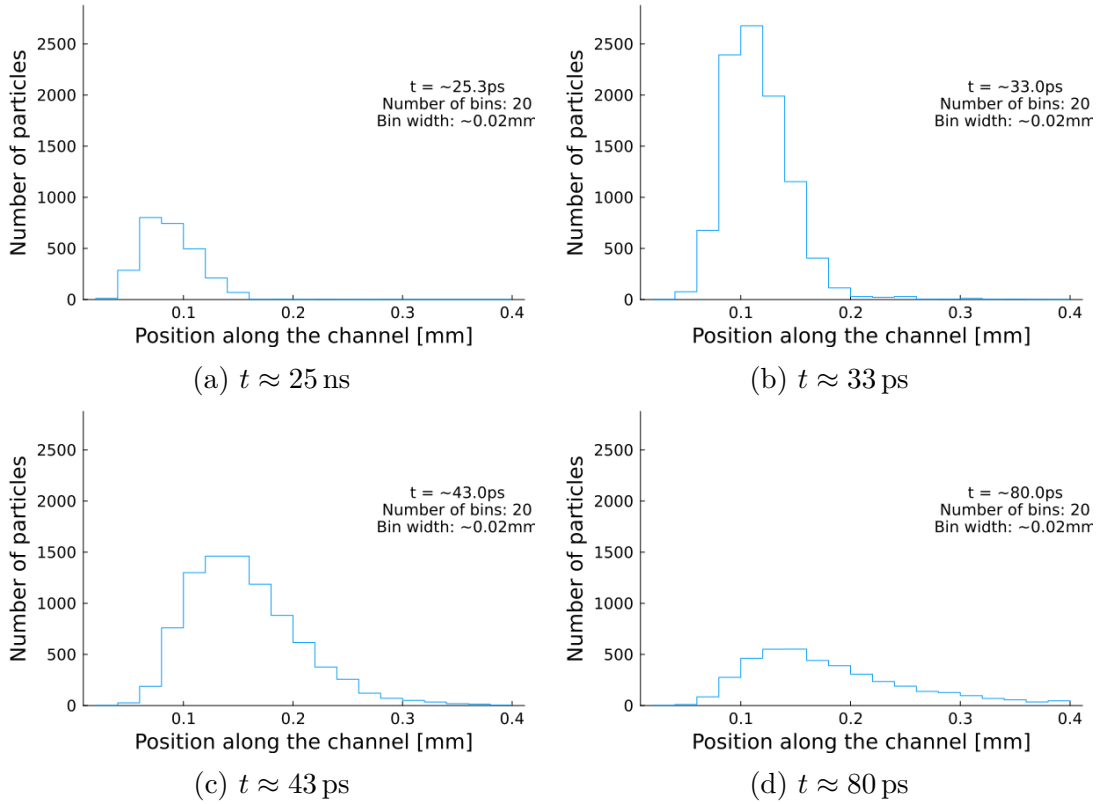

(a) $t \approx 25$ ns (b) $t \approx 33$ ps

(c) $t \approx 43$ ps (d) $t \approx 80$ ps

Figure 2.21: Histograms of the number of particles along the channel at different times. The Furman-Pivi model of secondary emission was used. These plots and the plots from Figure 2.20 are from the same run.

The histograms of the average speed of the particles of the particles, as shown

in Figure 2.22, can shed more light on the problem. The histograms were made by calculating the average speed of particles that were in a bin at some time t. The histograms show how the particles are accelerated by the electric field as expected. This means that the problem is with the direction of particle velocity.

The histogram in Figure 2.22b is not continuous. This is probably caused by fast-moving particles. Because the direction of the initial velocities is random, it can happen that the direction would be such that a particle would travel a long distance and can gain a lot of energy. Such particles would create high spikes in the histograms near the end of the microchannel. Indeed the histogram in Figure 2.22b contains such spikes. Figure 2.22 also shows how the distribution become linear over time. This is expected because as the particles propagate through the microchannel, they are accelerated by the electric field. The field is constant, which means that the acceleration of the particles is constant, so the speed increases linearly. They lose some energy in the collision, but usually it is not enough to significantly change this behaviour, or at least not in this simplified model. However, it can happen that an electron is absorbed by the channel wall. In that case, the electron is removed from the simulation, and it would not significantly alter the distribution in Figure 2.22.

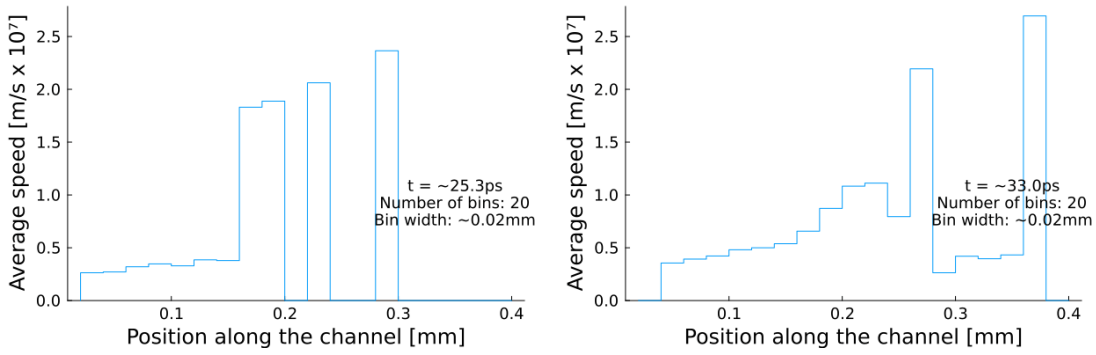

(a) $t \approx 25\,\text{ns}$

(b) $t \approx 33\,\text{ps}$

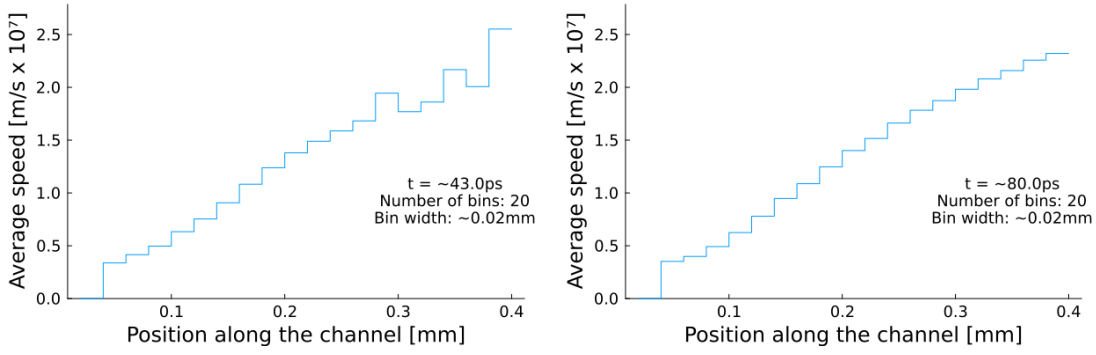

(c) $t \approx 43\,\text{ps}$

(d) $t \approx 80\,\text{ps}$

Figure 2.22: Histograms of the average speed of particles along the channel at different times. The Furman-Pivi model of secondary emission was used. These plots and the plots from Figure 2.20 are from the same run.

It is important to know how the electrons exit an MCP. The Figure 2.23 shows a 3D plot of the velocity vectors of electrons when they left the microchannel. The electric field used in the simulation was parallel with the channel axis, which means that the vectors should be symmetrically distributed around the end of the

channel. This is exactly what Figure 2.23 shows. It can be better seen from the 2D histogram in Figure 2.26a. The histogram also shows that the majority of the electrons have high speed. The high speed corresponds to the high energy of the output electrons, which can be seen from the energy distribution in Figure 2.24a. The distribution shows a minimum number of electrons with low energy and a high number of electrons with high energy. The maximum of the distribution is at $\sim 1.8\,\mathrm{keV}$. This is in strong disagreement with the typical distribution from Figure 2.10.

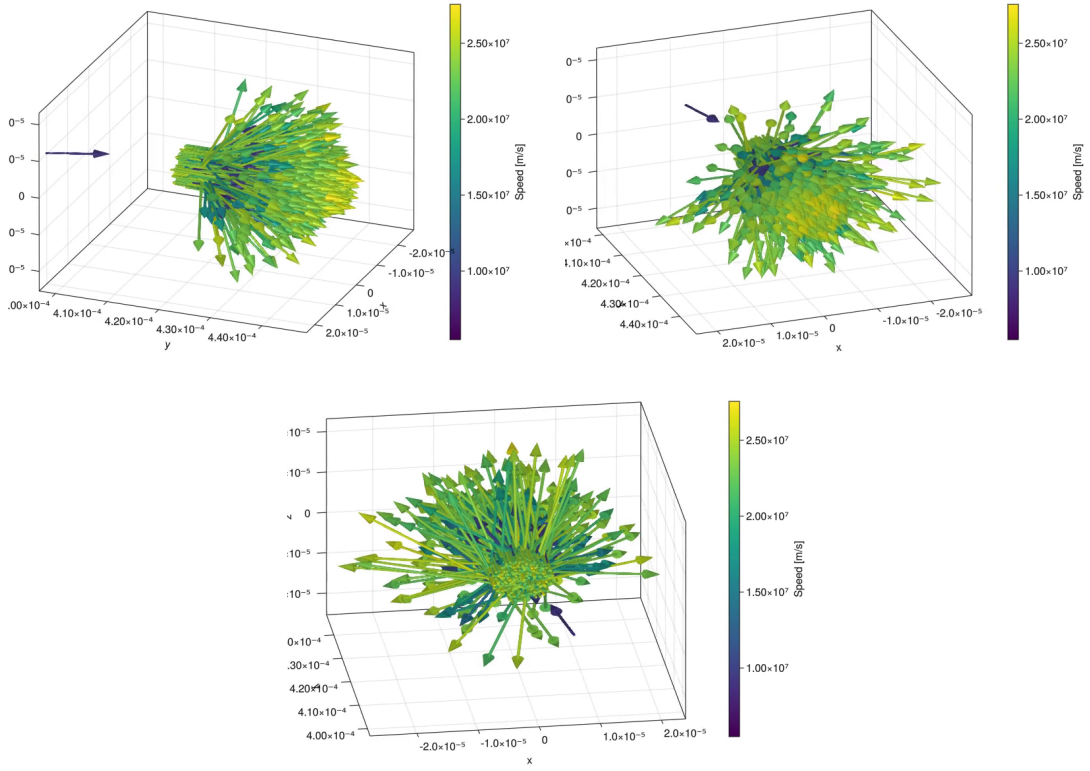

Figure 2.23: 3D plot of velocity vector of electrons exiting the microchannel.

Figure 2.26a also shows that the spread of the angle θ between the velocity and the channel axis is significant. However, the majority of the vectors are parallel to the axis. In the region around $2.5 \times 10^7\,\mathrm{m\,s^{-1}}$ the symmetry in the angle distribution can be loosely seen. It is not very pronounced, but it could be improved by a higher number of samples, which means introducing more particles into the simulation. The angle distribution of the output electrons in Figure 2.25a shows that the majority of the electrons exited the channel parallel to the channel axis. The measured angle distribution in Figure 2.27 shows that the majority of electrons exited the microchannel at some small angle. The distribution then drops, but is non-zero even at $\theta = 15°$. On the other hand, there should be almost no electrons exiting parallel to the microchannel.

The situation is also similar if the electric field is not parallel to the channel axis, but it is tilted by 15°. In this case, the distribution of the angle θ should not be symmetric because the electric field should push the electrons towards one side. Indeed the 2D histogram in Figure 2.26b shows a significant spread of the angles. Similarly to the histogram in Figure 2.26a, the histogram in Figure 2.26b

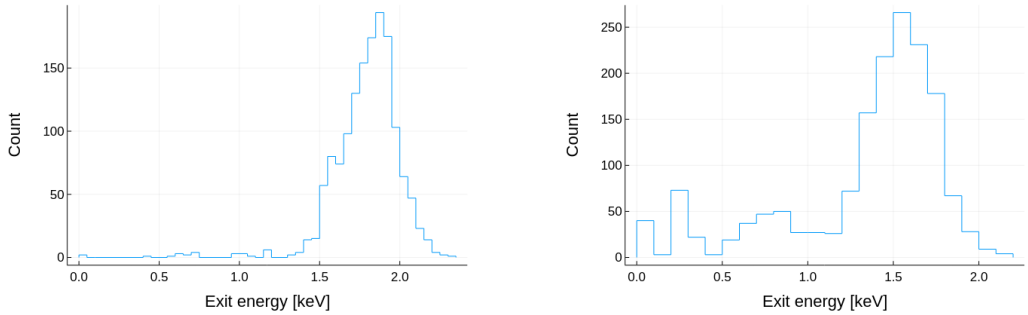

(a) For the case of parallel electric field.

(b) For the case of electric field tilted by 15°.

Figure 2.24: Energy distribution of the output electrons.

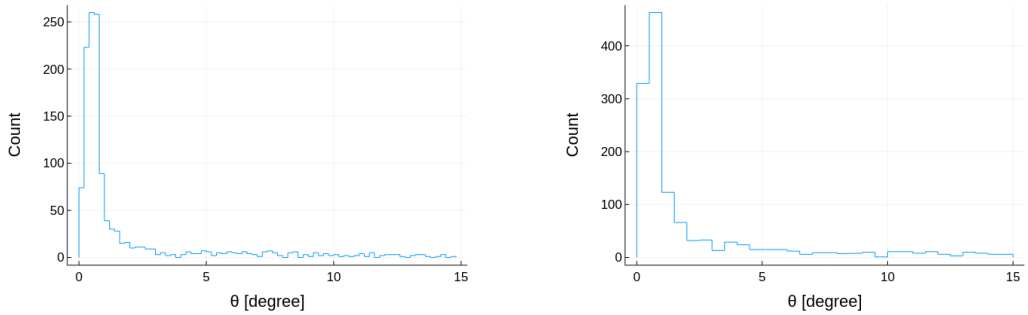

(a) For the case of parallel electric field.

(b) For the case of electric field tilted by 15°.

Figure 2.25: Angle distributions of the output electrons.

also shows a peak in the region with speed around $2.5 \times 10^7\,\mathrm{m\,s^{-1}}$, but it looks like there could be a second one in the region with speed around $1 \times 10^7\,\mathrm{m\,s^{-1}}$. More data points are needed to better see if it is true. The histogram in Figure 2.26b also shows that the overall speed of the particles is lower.

The energy distribution in Figure 2.24b shows some electrons with small energies, but the overall shape of the distribution is similar to the distribution from the case with the parallel field. The angle distribution in Figure 2.25b did not change much compared to the previous case.

The COMSOL® model is very simple and does not include many effects that occur in an MCP microchannel. The model does not consider any saturation effects, and it does not include the fringe fields. Also, the results show that the current state of the model has problems with the proper propagation of the electrons. The easiest way to improve the model is to include the fringe fields effect. Instead of hard coding the value of the electric field, it can be calculated by COMSOL®. This requires only a small modification of the geometry. The effects of ALD can be partially included by changing the parameters of the Furman-Pivi model. The addition of the saturation effects is more complicated because the wall charge density is not homogenous and how to represent it in the model needs

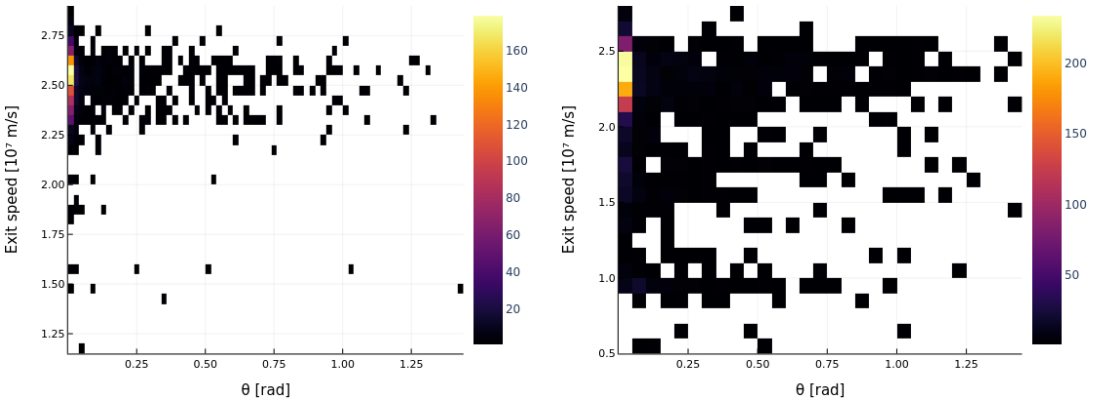

(a) The electric field was parallel to the channel axis.

(b) The electric field was tilted by 15°.

Figure 2.26: 2D histogram of speeds of electrons exiting the microchannel and the angle between their velocity vector and the channel axis.

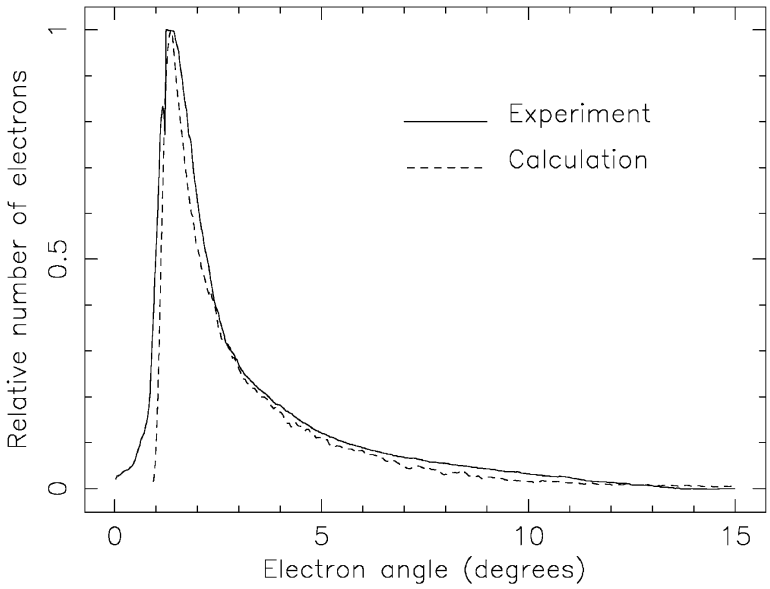

Figure 2.27: Measured angle distribution of output electrons. The calculated curve was created by the authors of the original paper [19] and is unrelated to this thesis.

to be investigated. However, the problem with the electron velocities should be addressed first because it renders the model unphysical.

Conclusion

This thesis describes the basic theory behind microchannel plate photomultipliers. However, the main goal of this thesis was to show different approaches to MCP-PMT simulations and to attempt to develop such simulations. It was shown that the TLM methods can be used for the simulations. It was also shown that the Guidiccotis' TLM model is insufficient to correctly simulate MCP-PMT. There was an attempt to use the calculation of the wall charge from Guidicotti's model in a different simulation, but it failed to reproduce expected results and it was not used at the end. Then the Monte Carlo method was introduced. Two simple models were developed. The quasianalytical model tried to optimize the computations by analytically solving the equations of motion. Then the Particle-In-Cell model was developed. The two models were compared, and it was shown that the PIC model could be more general because it could be used to simulate fringe field effects and particle interactions. Also, the difference between a simulation in 2D and 3D was shown. Unfortunately, the two models were unfinished because of the problems with memory and shortness of time. Instead, the use of COMSOL Multiphysics was investigated. A simple model of a single microchannel was created using the software. It was shown that the Firman-Pivi model of secondary emission can be incorporated into the COMSOL model. It was also shown that this model can be used to simulate the majority of effects occurring in MCPs. The software can be used to simulate fringe fields, particle interaction and saturation effects. Unfortunately, this model also shows problems, and in its current state, it does not reproduce the behaviour correctly. However, this model has the most potential. With more time, the problems could be solved, and more effects could be added to the model.

Acknowledgement

Computational resources were provided by the e-INFRA CZ project (ID:90254), supported by the Ministry of Education, Youth and Sports of the Czech Republic.

Bibliography

[1] Adamczyk, L. et al. Technical Design Report for the ATLAS Forward Proton Detector. Technical report, 2015.

[2] Flyckt, S.O. and Marmonier, C. *Photomultiplier tubes: principles and applications; 2nd ed.* Photonis, Brive, 2002.

[3] Committee, H.P.K.E. *PHOTOMULTIPLIER TUBES: Basics and Applications.* Hamamatsu Photonics K.K. Electron Tube Division, 4 edition, 2017.

[4] L., W.J. Nucl. instrum. methods. *Nucl. Instrum. Methods*, 62, 1979.

[5] Guest, A. A computer mode 01 channel multiplier plate performance. *Acta Electron*, 14:79, 1971.

[6] Adams, J. and Manley, B. The mechanism of channel electron multiplication. *IEEE transactions on nuclear science*, 13(3):88–99, 1966.

[7] Wiley, W. and Hendee, C. Electron multipliers utilizing continuous strip surfaces. *IRE Transactions on Nuclear Science*, 9(3):103–106, 1962.

[8] Gys, T. Micro-channel plate photon detectors. CERN Detector seminar, Feb 7, 2014.

[9] Pearson, J., Fraser, G. and Whiteley, M. Variation of microchannel plate resistance with temperature and applied voltage. *Nuclear Instruments and Methods in Physics Research Section A: Accelerators, Spectrometers, Detectors and Associated Equipment*, 258(2):270–274, 1987.

[10] Ivanov, V. et al. Numerical simulation of fast photo detectors based on microchannel plates. *Journal of Instrumentation*, 12(09):P09024, 2017.

[11] Chen, P. et al. Photoelectron backscattering in the microchannel plate photomultiplier tube. *Nuclear Instruments and Methods in Physics Research Section A: Accelerators, Spectrometers, Detectors and Associated Equipment*, 912:112–114, 2018. New Developments In Photodetection 2017.

[12] Shikhaliev, P. Saturation model for secondary electron multiplier detectors. *Nuclear Instruments and Methods in Physics Research Section A: Accelerators, Spectrometers, Detectors and Associated Equipment*, 420(1):202–212, 1999.

[13] Bryant, D.A. and Johnstone, A.D. Gain of a Channel Multiplier. *Review of Scientific Instruments*, 36(11):1662–1662, 12 2004.

[14] Barnyakov, A. et al. Photomultiplier tubes with three mcps. *Nuclear Instruments and Methods in Physics Research Section A: Accelerators, Spectrometers, Detectors and Associated Equipment*, 598(1):160–162, 2009. Instrumentation for Collding Beam Physics.

[15] Scholtz, J., Dijkkamp, D. and Schmitz, R. Secondary electron emission properties. *Philips Journal of Research*, 50(3):375–389, 1996. New Flat, Thin Display Technology.

[16] Furman, M. and Pivi, M. Probabilistic model for the simulation of secondary electron emission. *Physical review special topics-accelerators and beams*, 5(12):124404, 2002.

[17] Wulff, E. and Iadarola, G. Implementation and benchmarking of the furman-pivi model for secondary electron emission in the pyecloud simulation code. Technical report, 2019.

[18] Zhu, Y. et al. Study on fast timing mcp-pmt in magnetic fields from simulation and measurement. *Sensors and Actuators A: Physical*, 318:112487, 2021.

[19] Fraser, G. The gain, temporal resolution and magnetic-field immunity of microchannel plates. *Nuclear Instruments and Methods in Physics Research Section A: Accelerators, Spectrometers, Detectors and Associated Equipment*, 291(3):595–606, 1990.

[20] Bateman, J., Apsimon, R. and Barlow, F. A new photomultiplier tube utilising channel plate electron multipliers as the gain producing elements. *Nuclear Instruments and Methods*, 137(1):61–70, 1976.

[21] Gys, T. Micro-channel plates and vacuum detectors. *Nuclear Instruments and Methods in Physics Research Section A: Accelerators, Spectrometers, Detectors and Associated Equipment*, 787:254–260, 2015. New Developments in Photodetection NDIP14.

[22] Jinno, T. et al. Lifetime-extended mcp-pmt. *Nuclear Instruments and Methods in Physics Research Section A: Accelerators, Spectrometers, Detectors and Associated Equipment*, 629(1):111–117, 2011.

[23] Wada, T. et al. Influence of exposure to co, co2 and h2o on the stability of gaas photocathodes. *Japanese Journal of Applied Physics*, 29(10R):2087, oct 1990.

[24] Conneely, T.M., Milnes, J.S. and Howorth, J. Extended lifetime mcp-pmts: Characterisation and lifetime measurements of ald coated microchannel plates, in a sealed photomultiplier tube. *Nuclear Instruments and Methods in Physics Research Section A: Accelerators, Spectrometers, Detectors and Associated Equipment*, 732:388–391, 2013. Vienna Conference on Instrumentation 2013.

[25] Ertley, C. et al. Performance studies of atomic layer deposited microchannel plate electron multipliers. *Nuclear Instruments and Methods in Physics Research Section A: Accelerators, Spectrometers, Detectors and Associated Equipment*, 912:75–77, 2018. New Developments In Photodetection 2017.

[26] Popecki, M.A. et al. Microchannel plate fabrication using glass capillary arrays with atomic layer deposition films for resistance and gain. *Journal of Geophysical Research: Space Physics*, 121(8):7449–7460, 2016.

[27] Inami, K. Mcp-pmt production for belle ii top detector and further r&d. *Nuclear Instruments and Methods in Physics Research Section A: Accelerators, Spectrometers, Detectors and Associated Equipment*, 936:556–557, 2019. Frontier Detectors for Frontier Physics: 14th Pisa Meeting on Advanced Detectors.

[28] Inami, K. Top counter for particle identification at the belle ii experiment. *Nuclear Instruments and Methods in Physics Research Section A: Accelerators, Spectrometers, Detectors and Associated Equipment*, 766:5–8, 2014. RICH2013 Proceedings of the Eighth International Workshop on Ring Imaging Cherenkov Detectors Shonan, Kanagawa, Japan, December 2-6, 2013.

[29] Inami, K. Mcp-pmt development for belle-ii top counter. *Physics Procedia*, 37:683–690, 2012. Proceedings of the 2nd International Conference on Technology and Instrumentation in Particle Physics (TIPP 2011).

[30] Miehling, D. et al. Lifetime and performance of the very latest microchannel-plate photomultipliers. *Nuclear Instruments and Methods in Physics Research Section A: Accelerators, Spectrometers, Detectors and Associated Equipment*, 1049:168047, 2023.

[31] Christopoulos, C. *The transmission-line modeling method TLM*. IEEE/OUP Series on Electromagnetic Wave Theory. Institute of Electrical and Electronics Engineers, 1995.

[32] Giudicotti, L. et al. Simple analytical model of gain saturation in microchannel plate devices. *Review of Scientific Instruments*, 65(1):247–258, 01 1994.

[33] Giudicotti, L. Analytical, steady-state model of gain saturation in channel electron multipliers. *Nuclear Instruments and Methods in Physics Research Section A: Accelerators, Spectrometers, Detectors and Associated Equipment*, 480(2-3):670–679, 2002.

[34] Giudicotti, L. Time dependent model of gain saturation in microchannel plates and channel electron multipliers. *Nuclear instruments and methods in physics research section a: accelerators, spectrometers, detectors and associated equipment*, 659(1):336–347, 2011.

[35] Berkin, A. and Vasil'ev, V. A new approach to modeling current amplification in the channel of a microchannel plate. *Technical Physics Letters*, 33:664–666, 2007.

[36] Berkin, A. and Vasil'ev, V. Mathematical model of the direct current amplification mode in a channel of a microchannel plate. *Technical Physics*, 53:272–275, 2008.

[37] Malvin H. Kalos, P.A.W. *Monte Carlo Methods*. Wiley-VCH, 2 edition, 2008.

[38] Wolfram Research, Inc. Mathematica, Version 13.2. Champaign, IL, 2022.

[39] Tskhakaya, D. et al. The particle-in-cell method. *Contributions to Plasma Physics*, 47(8-9):563–594, 2007.

[40] Koshida, N., Midorikawa, M. and Kiuchi, Y. Output energy distribution of a microchannel plate. In Hawkes, P.W. and Morgan, B., editors, *Photo-Electronic Image Devices*, volume 64 of *Advances in Electronics and Electron Physics*, pages 337–342. Academic Press, 1985.

[41] Bezanson, J. et al. Julia: A fresh approach to numerical computing. *SIAM Review*, 59(1):65–98, 2017.

[42] Chen, J. and Revels, J. Robust benchmarking in noisy environments. *arXiv e-prints, arXiv:1608.04295*, Aug 2016.

[43] COMSOL AB, Stockholm, S. COMSOL multiphysics®. `https://www.comsol.com`. Accessed: 24. 6. 2023.

[44] COMSOL AB, Stockholm, S. The COMSOL product suite. `https://www.comsol.com/products`. Accessed: 24. 6. 2023.

[45] Ivanov, V., Insepov, Z. and Antipov, S. Simulation of gain and timing resolution in saturated pores. *Nuclear Instruments and Methods in Physics Research Section A: Accelerators, Spectrometers, Detectors and Associated Equipment*, 639(1):158–161, 2011.

[46] Löffler, J. et al. Monte carlo modeling of electron multiplication in amorphous silicon based microchannel plates. In *2019 IEEE Nuclear Science Symposium and Medical Imaging Conference (NSS/MIC)*, pages 1–6, 2019.

List of Figures

List of Tables

List of Abbreviations

PMT PhotoMultiplier Tube 2

MCP MicroChannel Plate 2

MCP-PMT MicroChannel Plate PhotoMultiplier Tube 2

ALD Atomic Layer Deposition 13

AFP ATLAS Forward Proton 2

ToF Time-of-Flight 2

SEY Secondary electron Emission Yield 10

PDF Probability Density Function 11

TLM Transmission Line Modeling 17

PIC Particle-In-Cell 1